Coal Fire Induced Land Subsidence Analysis by Integrated TIR and DInSAR Data Processing Approach

ISHAAN KOCHHAR
March, 2014

IIRS SUPERVISOR
Dr. R.S. Chatterjee

ITC SUPERVISOR
Dr. C.A. Hecker

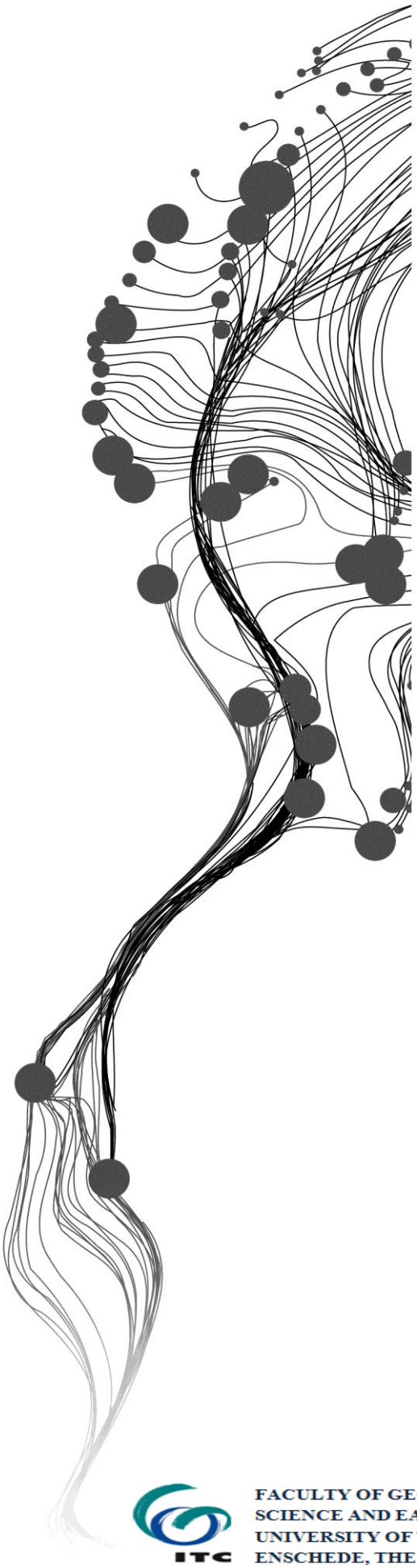

Coal Fire Induced Land Subsidence Analysis by Integrated TIR and DInSAR Data Processing Approach

ISHAAN KOCHHAR
Enschede, The Netherlands [March, 2014]

Thesis submitted to the Faculty of Geo-information Science and Earth Observation (ITC) of the University of Twente in partial fulfilment of the requirements for the degree of Master of Science in Geo-information Science and Earth Observation.
Specialization: Natural Hazards and Disaster Risk Management

THESIS ASSESSMENT BOARD:

Chairperson	: Prof. Dr. V. G. Jetten
External Examiner	: Prof. R.C. Lakhera (Retd. ISRO)
IIRS Supervisor	: Dr. R.S. Chatterjee
ITC Supervisor	: Dr. C.A Hecker

OBSERVERS:

ITC Observer	: Dr. N.A.S Hamm
IIRS Observer	: Dr. P.K. Champati Ray

FACULTY OF GEO-INFORMATION SCIENCE AND EARTH OBSERVATION, UNIVERSITY OF TWENTE, ENSCHEDE, THE NETHERLANDS

INDIAN INSTITUTE OF REMOTE SENSING
Indian Space Research Organisation
Department of Space, Government of India

DISCLAIMER

This document describes work undertaken as part of a programme of study at the Faculty of Geo-information Science and Earth Observation (ITC), University of Twente, The Netherlands. All views and opinions expressed therein remain the sole responsibility of the author, and do not necessarily represent those of the institute.

Dedicated to my family

ABSTRACT

In a coalfield, land subsidence can occur due to variety of causes such as underground mining, subsurface coal fires and vulnerability of old underground mine workings. This study explores the integrated approach by overlapping the results of TIR and DInSAR data processing techniques to separate and monitor the land subsidence affected areas due to coal fire. ASTER (90 m) thermal infrared (TIR) data is used to detect coal fire related thermal anomalies. Differential Interferometric Synthetic Aperture Radar (DInSAR) processing is carried out on ALOS PALSAR data to measure the surface deformations. Jharia Coal Field (J.C.F) in the state of Jharkhand (India) is taken as the study area. Coal fire dynamics were studied for different periods (October 2006 and November 2009). DInSAR was carried out from November 2007 to December 2010.Integrating the coal fire related thermal anomalies with the DInSAR derived land subsidence and the mining related database helped to delineate coal fire related subsidence. The analysis of the results in coal mining induced subsidence areas (F2 and F6) showed increase in the spatial extent whereas the coal fire related subsidence areas (fringe ID F4 and F5) showed decrease in their spatial coverage. Coal fire induced subsidence (F4 and F5) showed gradual decrease in the rate of deformation, whereas the mining induced subsidence showed gradual increase in the rate of subsidence at active mining site(F6) and increase in the rate of subsidence at other mining site (F2).

Keywords: DInSAR, InSAR, coal fire, land subsidence, Jharia coalfield, ASTER, ALOS PALSAR.

ACKNOWLEDGEMENTS

This thesis is the result of six months of work. It could not have been completed without the support and encouragement of a number of people. Since, it is impossible to thank them all, therefore I will mention only those without whom this study could never have been accomplished.

It was a great pleasure and enlightening to work with my IIRS supervisor and *guru* Dr. R.S. Chatterejee. Despite his very busy schedule, his door was always open for me for discussions. Without his active support, and critical comments, the research could not have been completed.

I am thankful to my ITC supervisor Dr. C.A. Hecker. His constant encouragement and support throughout my ITC stay cannot be expressed in few words. Without his valuable and timely comments it was nearly impossible to narrow down my ideas to reach the goal.

I would like to thank Dr. Y. V. N. Krishnamurthy (Director, IIRS) for providing the support and infrastructure needed for the implementation of this project. Special thanks to the course co-ordinator and head of Geoscience and Geo-hazards Department (GSGHD), Dr. P.K. Chamapti Ray for his caring attitude towards students and providing valuable advices.
I gratefully acknowledge the academic and technical support from Shailja Thapa and Ashish Dhiman.
My heartfelt thanks and gratitude go to Shreya Khatri, Azzedine Salhi, Saleem Malik, Sajid Anwar, Kanishk, Aravind, Ravisha, Shreya Chandola, Deepak, Hemlata, Guru, Piyush, Shishant, Shashi, Manjeet, Saurabh, Mahesh, and three Viveks ☺.
Finally I would like to thank my family and Khatri family for their inspiration, moral support and love which enabled me to complete this work.

Ishaan Kochhar
Dehradun, March, 2014

TABLE OF CONTENTS

LIST OF FIGURES

LIST OF TABLES

1. INTRODUCTION

1.1. Background

Natural resources are the backbone of the economy. Mining of these natural resources is carried out worldwide. However various hazards are triggered due to mining of natural resources. One such natural resource is coal, which is a non-renewable source of energy. Mining of coal is carried out for centuries because of its numerous benefits such as source of fuel, electricity etc. Hazards associated to coal mining are for example, land subsidence, surface and subsurface coal-fires.

1.1.1. Land subsidence and coal fires

Land subsidence may be defined as "the gradual and/or sudden sinking of landforms to a lower level as a result of a subsurface movement of earth materials" (Zeitoun & Wakshal, 2013).

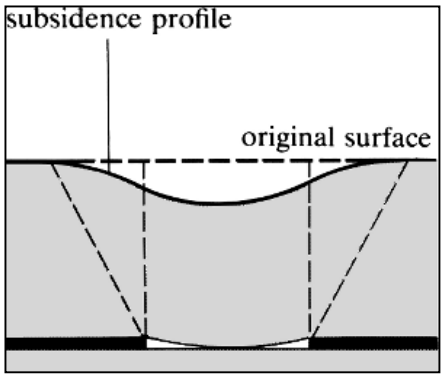

Figure 1-1: Mechanism of subsidence. Source (Brady & Brown, 2006)

In the coal fields, land subsidence is caused by various factors, which includes:

- Mining of coal in an unplanned manner where extraction of material from below the surface removes the adequate support from the overlying rocks resulting in surface collapse.
- In the past few decades, subsurface coal-fires have also been found as one of the subsidence causing problems.

Underground coal fires can start by spontaneous ignition of coal dust or methane gas released from the coal. Such fires are difficult to extinguish. Burning of the coal reduces the volume which causes the surface displacements. The problem of coal fires is further ignited by mining as well as fires themselves. Open cracks and fissures in the land surface serves as inlets for oxygen(Prakash, Fielding, Gens, Van Genderen, & Evans, 2001). As the burned coal turns into ash, often the rock overburden can no longer be supported and deep cracks open up. Eventually, the overburden collapses causing huge damage to surface, buildings, transport network, etc.(Gangopadhyay, Maathuis, & Van Dijk, 2005).

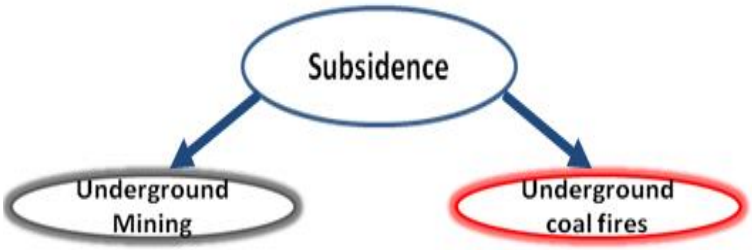

Figure 1-2: Possible causes of subsidence in study area.

Many countries around the world are affected by coal fires. Some of the countries facing the issue of coal fire where coal fires have been identified and monitored are China (Gangopadhyay et al., 2005), India (Chatterjee et al., 2007), Australia (Ellyett & Fleming, 1974). The burning of coal fields is a worldwide challenge and it has been observed that the subsurface coal fires have been active for many years which had already affected tons of valuable coal reserve deposits.

Some of the effects of coal fire are listed below:

- Large amount of toxic and greenhouse gases, such as SO_2, NO, CO, CH_4 and CO_2, are emitted from the fires polluting the air(Voigt et al., 2004) resulting in degradation of the environment and millions of people are affected due to coal-fires causing health related problems.
- Land deformations caused by underground coal fires affect the nearby human settlements.
- It also obstructs further mining process. Burning of valuable coal deposits causes huge economic loss.

For the sustainable development of the mining environment, the socio-economic impacts, environmental impacts, health and safety issues of the local people requires methods for monitoring and controlling fires and land subsidence from expanding further.

1.2. Coal fires and remote sensing

To map the thermal radiation emitted by coal fires space borne satellite remote sensing is an effective tool. Studies by using this technique have shown that mapping and monitoring of coal fires, using space borne thermal infrared(TIR) data show up hotspots, changes in terms of spatial coverage and propagation of coal fires (Gangopadhyay et al., 2005), (Chatterjee, 2006), (C. Kuenzer, Hecker, Zhang, Wessling, & Wagner, 2008), (Chatterjee et al., 2007). However mixing of false alarms such as industrial units with the thermal anomalies of coal fires is a limiting factor of coal fire thermal anomaly detection techniques. Water bodies such as lakes, rivers also appear as thermal anomalies while mapping coal fires (C. Kuenzer et al., 2008).Thermal remote sensing is a technique uses infrared region of electromagnetic spectrum.

In thermal remote sensing, temperature estimations are made by measuring the radiation emitted by ground objects.Thermal infrared (TIR) data is being used in a broad variety of fields for example to assess land or sea-surface temperature dynamics, detect forest, coal and peat fires, map urban heat islands etc.(Claudia Kuenzer & Dech, 2013).

1.3. Land subsidence and remote sensing

Differential Interferometric Synthetic Aperture Radar (DInSAR) is a tool for determination of subsidence, uplifting and shifting of earth's surface with a capability of measuring very small deformations in terrain with up to 1 cm precision (Gabriel, Goldstein, & Zebker, 1989). DInSAR has the potential to determine deformations and topographic changes on the earth's surface due to earthquake, landslides, land subsidence, glacier movements(Zeitoun & Wakshal, 2013), (Motagh et al., 2008), (Tomás et al., 2013). The technique determines topographic changes which are derived from phase information contained in multiple radar images acquired at different times. The technique determines topographic changes which are derived from phase information contained in multiple radar images acquired at different times. In view of the fact that DInSAR contains only phase information, it is difficult to separate out subsidence due to coal fires and subsidence due to mining activities from the phase information (Voigt et al., 2004), (Zhou, Zhang, Wang, Huang, & Pan, 2013).

Synergistic use of two different remote sensing techniques by integrating thermal infrared (TIR) for thermal anomaly detection and DInSAR for land subsidence measurements is required. Study of multi-temporal TIR dataset provides information on dynamics of underground coal fires in addition to their spatial extent. Multi-temporal analysis of SAR images will provide us the spatio-temporal development of the subsidence and the speed in which it progresses. Therefore to study the land subsidence characteristics in relation to spatio-temporal dynamics of coal fire an approach by integrating TIR and DInSAR data processing approach is proposed. The land subsidence characteristics to be explored in the research are the rate and type of surface deformation in the underground coal fire combustion areas with the development of coal fire which would help us to find out the relation of subsidence with coal fire.

With this the study aims to differentiate land subsidence resulting from coal fires and those resulting from ordinary mining activities in the study area. The research also aims to measure the rate of subsidence and the extent of coal fire by integrated TIR and differential radar interferometry approach. Finally the characteristics of coal fire induced subsidence and the characteristics of ordinary coal mining activities will be compared.

1.4. Research Identification

1.4.1. Research Objective

The main objective of the research is to study the land subsidence characteristics in relation to spatio-temporal dynamics of coal fire.

1.4.2. Sub-objectives

- To detect and delineate surface and subsurface coal fires from multispectral night time TIR data.

- To decipher spatio-temporal dynamics of coal-fire from multi-temporal TIR data.
- To delineate coal-fire induced land subsidence areas by combining DInSAR based subsidence maps with thermal anomaly maps.
- To investigate the characteristics of coal-fire induced land subsidence in comparison to coal mining induced land subsidence.
- To test if the temporal development of two subsidence types are significantly different from each other in DInSAR processing alone.

1.4.3. Research questions

- How well can we map thermal anomalies from ASTER data?
- Do all the coal fires detected show subsidence? What is the contribution of coal fire induced subsidence to overall subsidence scenario in the coalfield?
- How well do the deformation observed coincide with active fire?
- What is the nature of subsidence, gradual or sudden?
- How the spatial extent and the rate of subsidence vary in relation to spatio-temporal dynamics of coal-fire?
- How the spatio-temporal characteristics of coal-fire induced land subsidence differ from mining induced land subsidence?
- What is the influence of subsidence on the development of coal fires and what are the possible governing factors?

1.5. Scintific siginificane and innovative aspects

The uniqueness in this study is to use an integrated data processing approach combining Synthetic Aperture Radar (SAR) and thermal infrared (TIR) data.

"Thermal Infrared + DInSAR"

The integrated TIR and DInSAR data processing approach here is to analyse the characteristics of coal fire induced land subsidence by studying the spatial dynamics and the rate of subsidence which will improve the separation of subsidence affected areas occurred due to coal mining and subsurface coal-fires.

1.6. Potential use or users of the result

Uncontrollable spread of underground fires that have been burning for years in the Jharia coal field release poisonous smoke. Habitants near Jharia coal field have developed many health complications due to poor air quality. Coal fires generally increase the temperature of the surrounding areas (Prakash, Gupta, & Saraf, 1997). Urban and human settlements (buildings, road and railway networks etc.) in and around Jharia are facing the threat of subsidence. Subsidence issues have not only affected the surface properties but also caused financial and social problems in the society. Burning of fires beneath the ground and subsidence phenomena related to it pose serious challenge to the scientific community. The results of this study would help to better assess and monitor the coal fire and its related subsidence phenomenon.

1.7. Thesis structure

The work has been divided into seven chapters. The structure of the thesis is discussed in the following table:

Table 1-1: The structure of thesis

Chapter	Description
Chapter 1	Presents general overview about the research work. It describes the basic idea of topic, research objectives, and research questions.
Chapter 2	Deals with theoretical background of the study and literature review.
Chapter 3	Describes the study area and its attributes.
Chapter 4	Describes about dataset used.
Chapter 5	Describes the complete workflow of the study and description in details.
Chapter 6	Describes the experiments on selected data, achieved results, its discussion and analysis.
Chapter 7	Describes the answer of the research questions in concluded form and recommendations for further study.

2. THEORY AND LITERATURE REVIEW

2.1. Thermal infrared remote sensing

Thermal remote sensing is the branch of remote sensing that deals with the acquisition, processing and interpretation of data acquired primarily in the thermal infrared (TIR) region (3 to 15 μm) of the electromagnetic (EM) spectrum. Atmospheric windows in the range 3 to 5 μm and 8 to 14 μm are used by TIR remote sensing, because these parts of electromagnetic spectrum are not affected by atmospheric interaction. All objects with a temperature above absolute zero (0 Kelvin, which equals -273.15°C) emit electromagnetic radiation (Claudia Kuenzer & Dech, 2013).
In thermal remote sensing we measure the radiation emitted from the surface of the target, whereas in optical remote sensing we measure the radiation reflected by the target under consideration. Radiation emitted by ground objects are measured for temperature estimation.
TIR remote sensing has an advantage that data can be acquired independent of the sun as an illumination source. So thermal data can also be acquired during the night, when remote sensing in the visible and near infrared (NIR) is not possible. Night time TIR data is preferable for the study because with afternoon data, solar masking effects obstruct the extraction of many anomalies.
Remote sensing sensors responsive in the thermal domain have the ability to record this TIR radiation. The temperature of the surface over a coal fire depends on various factors.

2.1.1. Heat temperature, radiant flux and heat transfer

The energy released by particles of matter in a random motion is called kinetic heat. The random motion between the particles triggers collision, which results in change of energy state and the emission of electromagnetic radiation from surface of materials. The internal, or kinetic, heat energy of matter is thus converted into radiant energy.
Temperature is a measure of the concentration of heat. The Kelvin and Celcius scales relates as follows:
$T_c = T_k + 273.15$
Where T_c is the temperature in celcius and T_k is the temperature in Kelvin
The surface of materials emits electromagnetic energy, which is known as radiant flux and is measured in watts per square centimetre. The concentration of kinetic heat of a material is kinetic temperature and is measured with a thermometer placed in direct contact with the material. The concentration of a radiant flux of a body is the radiant temperature. The radiant temperature is always equal or less than the kinetic temperature because of a thermal property called emissivity, which is defined as radiant flux from a real material divided by the radiant flux from a blackbody. A thermal material that absorbs all radiant energy that falls on it is termed as blackbody.
Heat energy is transferred from one place to another by three means:

Table 2-1: Different modes of heat transfer

Sr. No	Heat Energy	Mode of Transfer
1	Conduction	Transfers heat through a material by molecular contact.
2	Convection	Transfers heat through physical movement of heated matter.
3	Radiation	Transfers heat in the form of electromagnetic waves

2.1.2. Stefan-Boltzman Law

It describes the total electromagnetic radiation emitted by a blackbody as a function of the absolute temperature of that blackbody (Claudia Kuenzer & Dech, 2013).
The area under the radiation curve corresponds to emitted radiation.

$$T_{RadBB} = \frac{1}{4}\sigma T_{kin^4} \quad (2\text{-}1)$$

T_{RadBB} = radiant flux of a blackbody [W/m^2],
T = absolute kinetic temperature [K],
σ = Stefan-Boltzmann constant [$5.6697 * 10^{-8}$ Wm^{-2} K^{-4}]

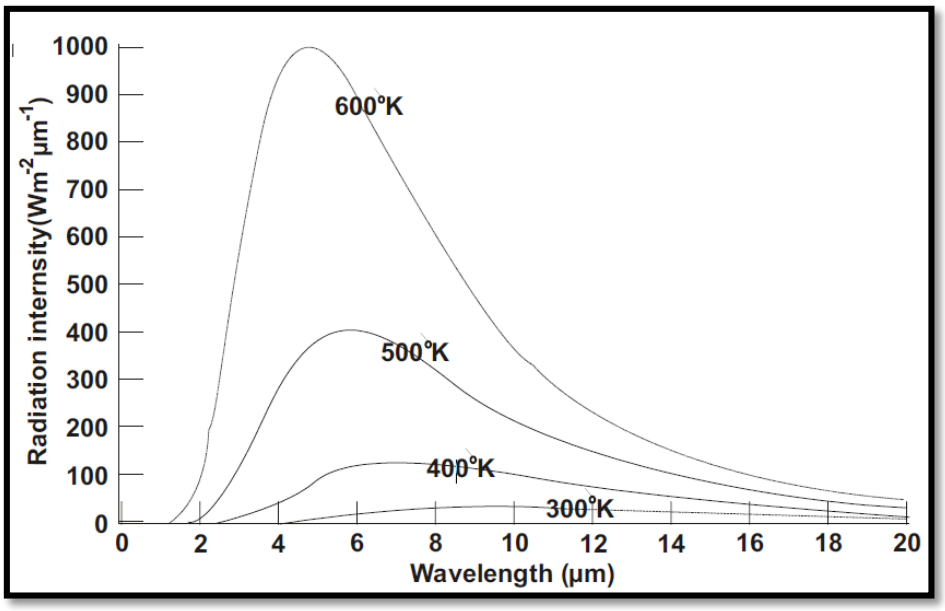

Figure 2-1: Relation between the wavelengths and rise in temperature. Source (J. Zhang, 2004)

The equation (2.1) shows that the higher the temperature of the radiating object the greater the total amount of radiation (energy) it emits. The equation has a non-linear relation; radiance is proportional to the fourth power of the black body's temperature.

2.2. InSAR

SAR systems record both amplitude and phase of the backscattered echoes. The main principle of Interferometric Synthetic Aperture Radar (InSAR) is to use the phase information of the backscattered echoes. InSAR technique uses phase of two SAR images, acquired at nearly same incident angle. The two SAR images are combined to generate a phase difference image called interferogram having a number of interference fringes (Li & Goldstein, 1990).

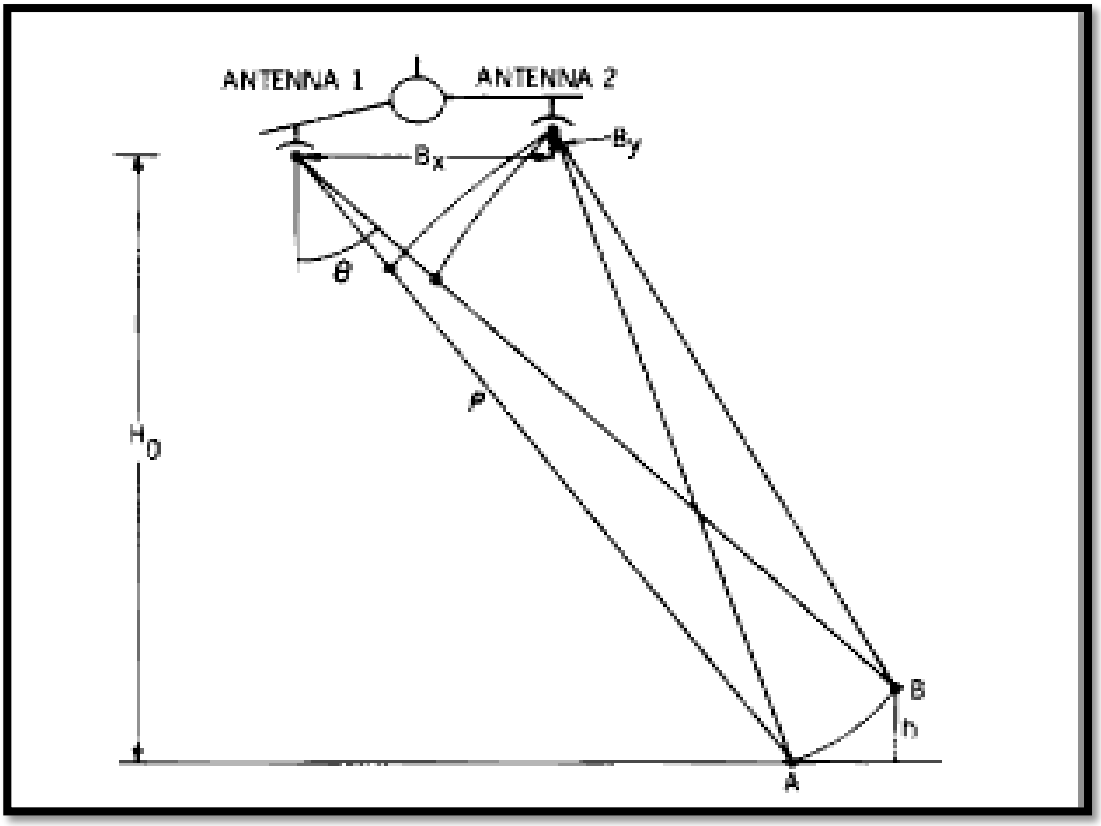

Figure 2-2: Airborne InSAR imaging geometry with two antennae. Source (Li & Goldstein, 1990)

The Figure (2-1) describing the imaging geometry of InSAR demonstrates that the target A and B will appear in same pixel in a SAR image. The targets have the same slant range to antenna 1 and are in the same relative azimuth position and therefore the backscattered echoes are projected to same pixel. Consequently it cannot measure the topographic height of the objects.

Two physical antennas are used to form interferometer, which are separated by baseline corresponding to a fraction of the aircraft dimension. The phase of the backscattered echoes recorded by the two antennae (1 and 2) will differ for the targets A and B. So for each pixel, the height of the object can be measured based on the phase differences.

The height of the target B with respect to the terrain is calculated as:

$$\Phi = \frac{4\pi}{\lambda} \left[Bx\ sin\theta - By\ cos\theta \right] \quad (2\text{-}2)$$

$$h = H_0 - \rho\cos\theta \quad (2\text{-}3)$$

where,

Φ is the phase difference

H is the height of the target B

H_0 is the flying height

ρ is the range from antenna A1 to the point on the ground

θ is the look angle

λ is the RADAR signal wavelength

B_x is baseline length between antenna1 and antenna 2

B_y is the vertical distance from intersecting point of horizontal from antenna1 and vertical from antenna2

The height (h) is computed using equation (2.3) based on the phase difference (Φ) and (θ).

2.3. DInSAR

Topographic mapping was one of the early applications of radar interferometry. InSAR had become a very effective tool for this application because the relative line of sight movement of point scatterers with respect to reference locations on the image could be measured as a fraction of wavelength. Space borne InSAR has become a widely accepted and effective tool to map surface movements, ground deformations, mining activities and volcano dynamics (Jiang, Lin, Ma, Kong, & Wang, 2011)

Developments in interferometry results many applications. One such well known application is deformation monitoring. However the limitation of interferometry is that, it fails when the effective baseline between the image pairs become greater than zero. Differential interferometry was the solution to this technique.

Three pass DInSAR technique was first introduced by Zebker et al.(Zebker, Rosen, Goldstein, Gabriel, & Werner, 1994).This technique uses three images of the same area to generate displacement map of the region. The three pass DInSAR technique described in the paper (Zebker et al., 1994) is shown:

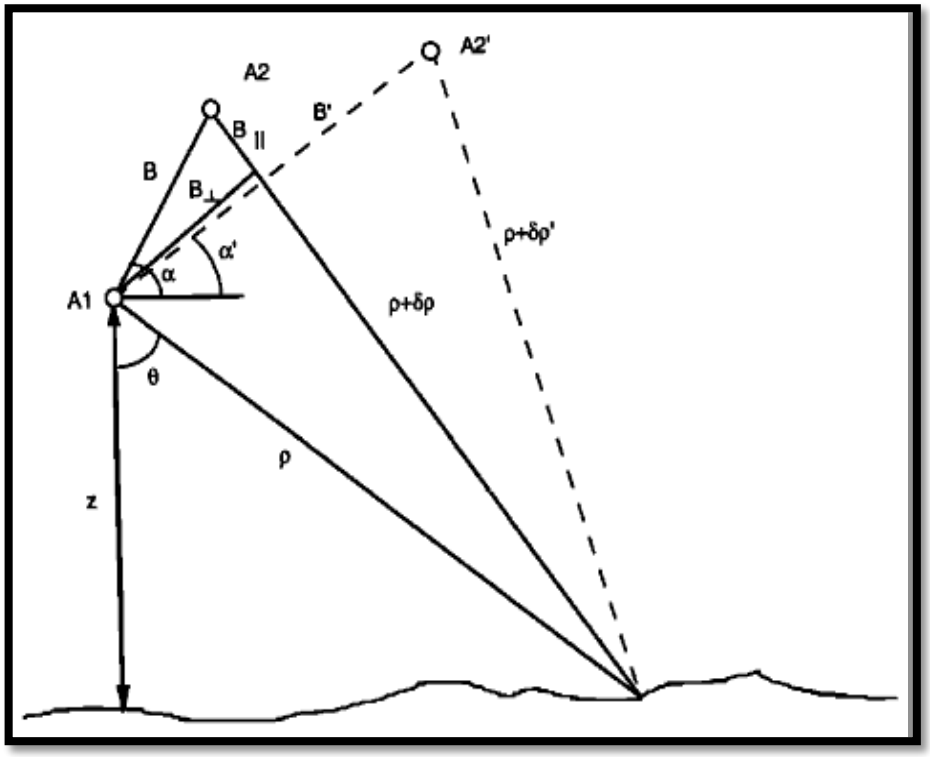

Figure 2-3: Three pass SAR geometry. Source (Zebker et al., 1994)

The Figure (2-3) demonstrates the imaging geometry of three pass SAR technique.The first interferogram pair is formed by antennas at A1 and A2 and the second interferogram pair is formed by antennas at A1 and A2'. The signals are acquired for the same site, however the antennas A2 and A2' are located at different locations. The solid lines denote the signal path for the first interferogram and the dashed lines indicate the signal path for the second interferogram. DInSAR phase equations are explained as:

$$\Phi_1 = \frac{4\pi}{\lambda}\rho \tag{2-4}$$

$$\Phi_2 = 4(\rho + \delta\rho) \tag{2-5}$$

$$\Phi_3 = 4(\rho + \delta\rho') \tag{2-6}$$

Where Ψ_1, Ψ_2,$\Psi_3$are the phases calculated from A1, A2 and A2' antenna positions to the ground points ρ, (ρ +δ ρ) and(ρ +δ ρ ').

λ is the RADAR signal wavelength.

From the three phase measurements derived, the Interferometric phases are derived as:

$$\Phi_1 = \Psi_1 - \Psi_2 = 4\pi\lambda\delta\rho \tag{2-7}$$

$$\Phi_2 = \Psi_1 - \Psi_3 = 4\pi\lambda\delta\rho' \tag{2-8}$$

From the Fig 2.3.based on the cosine law, the solution for δ ρ is formulated in (Zebker et al., 1994)as:

$$(\rho + \delta\rho)^2 = \rho^2 + B^2 - 2\rho B\sin(\theta - \alpha) \quad (2\text{-}9)$$

Where B is the baseline length
ϱ is the range from antenna A1 to the point on the ground
θ is the look angle
α is the angle of the baseline with respect to the sensor horizontal
From the equation, neglecting the $(\delta\rho)^2$ order term, the modified equation turns into:

$$\delta\rho \approx B\sin(\theta - \alpha) + \frac{B^2}{2\rho} \quad (2\text{-}10)$$

According to (Zebker et al., 1994) for space geometries, the second term in the eq.() can be neglected. Hence the equation becomes:

$$\delta\rho \approx B\sin(\theta - \alpha) \quad (2\text{-}11)$$

From the Fig.[2.2].

$$B\sin(\theta - \alpha) = B_{\parallel} \quad (2\text{-}12)$$

Therefore,

$$\delta\rho \approx B_{\parallel} \quad (2\text{-}13)$$

So, the final Interferometric phases are formulised as:

$$\Phi 1 = \frac{4\pi}{\lambda} B_{\parallel} \quad (2\text{-}14)$$

B'‖ is the baseline length of the second Interferometric pair. Consider the situation when displacement has occurred during the second Interferometric pair acquisition. Hence in addition to the topographic phase, an additional phase change due to displacement in the RADAR line of sight is also present (Zebker et al., 1994). So the second Interferometric phase is represented as:

$$\Phi 2 = \frac{4\pi}{\lambda}(B'_{\parallel} + \Delta\rho) \quad (2\text{-}15)$$

Where, Δϱ is the additional displacement component
From the equation (2.14) and (2.15), derive the deformation component as:

$$\Delta\rho = \frac{\lambda}{4\pi}\left[\Phi 2 - \left(\frac{B'_{\parallel}}{B_{\parallel}}\right)\Phi_1\right]$$

2.4. Related work

Earlier works on identification and analysis of coal-fires in Jharia coal fields were based on optical, multispectral, infrared data(Chatterjee, 2006),(Chatterjee et al., 2007). The dynamics of coal fire were studied using night time Landsat-5 TM thermal infrared (TIR) and shortwave infrared (SWIR) data and day time Landsat-7 ETM+ TIR data in terms of changes in spatial extent of fire affected areas and propagation of coal fire in (Chatterjee et al., 2007).

Analysis of multi-diurnal low resolution Moderate Resolution Imaging Spectroradiometer (MODIS) thermal data for coal fire-related thermal anomaly detection in Jharia coal fields was performed by(C. Kuenzer et al., 2008).The study combined three approaches: first, use of low-resolution MODIS data for coal fire area analyses. Second, data from four different times of day (morning, afternoon, evening and predawn) and for three different bands (MODIS bands 20, 32 and a ratio thereof) was analysed. Third, for thermal anomaly extraction of local thermal anomalies an unbiased automated algorithm was used. The analysis of MODIS multi-diurnal data indicated that evening and predawn data are more suitable for thermal anomaly extraction and also bands 20, 32 and ratio bands thereof, have a high potential for the detection of coal fire hot spot zones. It also concluded that the data utilized in the study is not suitable for a quantitative coal fire analysis in relation to fire outline, fire temperature or fire classification into surface and subsurface fires.

Study using ASTER data in combination with a Temperature/ Emissivity separation (TES) algorithms to estimate the surface temperature (Gangopadhyay et al., 2005) demonstrated the capabilities of ASTER data for detecting coal fire thermal anomalies in comparison to ground observations in Wuda coal fields, China. The TES algorithms used were Reference Channel Method (RCM) and Normalised Emissivity Method (NEM). Using TES approach, it was observed that ASTER based thermal anomalies corresponded well (accuracy$\pm$ 15℃) with actual measurements.

Previous study for the investigation of surface elevation changes in the Jharia coal fields was carried out by (Gupta, Mohanty, Kumar, & Banerjee, 2013). Investigation was performed by generating digital elevation model (DEM) using synthetic aperture radar interferometry (InSAR) using ERS-1/2 (European Remote Sensing Satellite) tandem and RADARSAT-1 data. The accuracy of the DEM was examined by comparing the elevation profiles with the digitized elevation contour data. Results showed that the InSAR derived heights and topographic heights were comparable (with root mean square error of $\pm$2.3m). It also demonstrated the capability of DEM generated using InSAR due to its high spatial details is ideal for the detection and estimation of surface elevation changes in mining areas. On the other hand it was not possible to measure the rate of deformation of the ground terrain using this technique.

Consequently DInSAR has proven to be an effective technique for detection and measurement of land subsidence due to exploitation of groundwater (Fan, Deng, Ju, Zhu, & Xue, 2011) , mining activities (Yang, Zhang, Zhao, Ji, & Zhu, 2010),(Dong, Yin, Yao, & Zhang, 2013). A case study was performed in Spain (Tomás et al., 2013) reviewing DInSAR data utilization related to ground subsidence phenomenon (groundwater, mining, soil compaction and evaporate dissolution subsidence) and addressing the investigation of active subsidence with DInSAR techniques in terms of spatial and temporal resolution, precision of the measurements, and utility of the data.

Land subsidence and coal fire hazards in a coal mining area (the Ruqigou coal field in the Hui Autonomous region in the north-west China) using data fusion techniques was investigated by (Prakash et al., 2001).The data used for the study was Landsat Thematic Mapper (TM), Landsat TM thermal infrared band (TM band 6), ERS-1 Synthetic Aperture Radar(SAR) images, Digital Elevation Model (DEM) with spatial resolution of 90 m and field data collected was GPS measurements, thermal profiles and field photographs. Fusion product of optical, thermal and microwave data was represented in False Color Composite(FCC) to represent three different pieces of information in three different colors (red for coal fires, blue for coherence from InSAR and green for subsidence areas). It was estimated that most of the fires which fall within the area of low correlation have large role in causing subsidence. On the other hand from the fusion product, in areas of very low correlation, the phase information could not be determined and quantitative estimation of the range change could not be performed.

An integrated remote sensing approach was used by (Voigt et al., 2004) to detect, analyze and monitor near surface coal seam fires by observing land surface changes (in thermal surface anomalies, spectral surface characteristics and land subsidence) induced by the fires in the Rujigou coal field, the Wuda coal field, the Ke-erJian coal field and Tielieke coal field respectively. ERS data acquired during tandem mission of the ERS-1/2 satellites was used to estimate surface subsidence rates by means of DInSAR. Landsat-7 ETM data was used for multispectral characterization of coal surface properties. MODIS, BIRD, ASTER and ETM data were used for thermal analyses of coal fires. This approach was able to detect and analyze mature and developed coal fires but has a limitation of not detecting very small and young fires. Also it does not differentiate land subsidence affects resulting from coal fires and those resulting from other subsidence sources.

Another method was exploited by (Zhou et al., 2013) to reveal the spatial and temporal behavior of large and highly non-linear subsidence induced by underground coal fires in Wuda coal fields, China. The ALOS PALSAR L- band data from Japan Aerospace Exploration Agency (JAXA) was used in the study for DInSAR processing. The coal fire distributions mapped in field work in 2008 and thermal anomaly contours generated using ETM scenes from October 2006 to September 2009 were overlaid with DInSAR results between October 2006 and January 2008. It provided a spatial extent and temporal evolution of the land subsidence behavior accompanying the coal fires. The study also showed significant potential of ALOS PALSAR data to detect land subsidence of interest. However the study was not able to show how two subsidence types (coal fire induced land subsidence and coal mining induced subsidence) are different from each other.

3. STUDY AREA

The study area consist of Jharia coalfield in the state of Jharkhand.It is located in the eastern part of India. The area is bounded between 23°40'00" to 23°50'00" N latitude and 86°10'00" to 86°30'00" E longitude covering an area of 450 km² approximately. The major city located in the study area is Dhanbad which is also known as the "Coal Capital of India". Other townships surrounding Dhanbad are Maheshpur, Katrasgarh in the north, Jharia, Dobari in the east. It is also surrounded by Katri river in the east and Damodar river in the south.

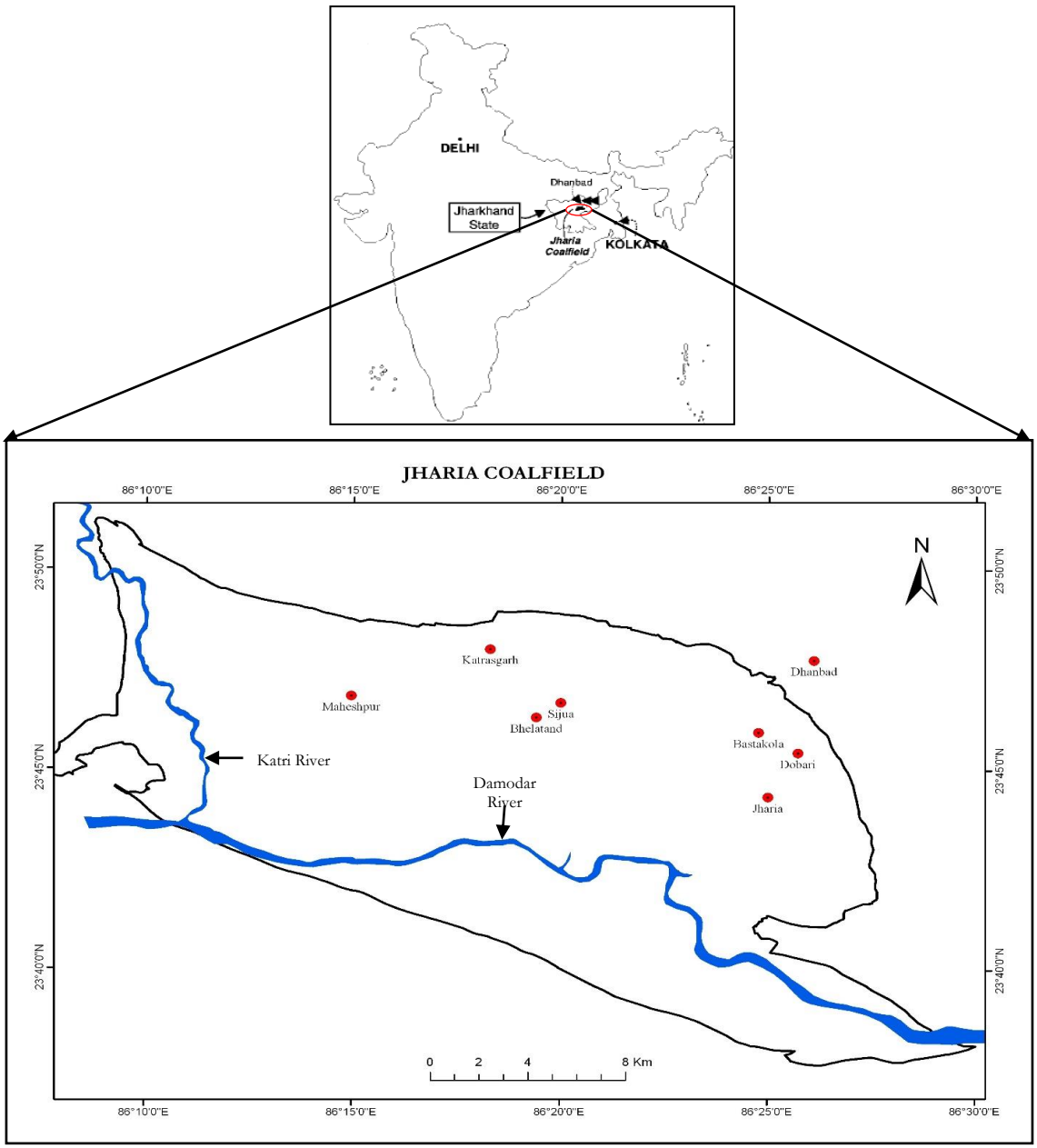

Figure 3-1: Geographical area of study area

3.1. Attributes of study area

1. It consists of mainly sedimentary rocks.
2. The major river in the study area is Damodar which flows in the south of this coal filed.
3. This coal field has more than 100 coal mines.
4. In this coal field there are underground mining activities and also opencast mining activities. But, major mining procedure is done by opencast mining method.
5. Underground mining areas are densely populated and population in affected areas is high which approximates to 1.1 million which are facing problems like resettlement and rehabilitation.
6. The coal field has three main coal formations namely
    a) Barakar,
    b) Barren measures and
    c) Raniganj formations.

Barakar and Raniganj formations are coal bearing but Barren measure is a non-coal bearing formation.

3.2. Geology of study area

3.2.1. Coal reserves of Jharia Coalfield (J.C.F) and reclamation measures adopted

Within the leasehold of Bharat Coking Coal Limited (BCCL), the geological coal reserves of Jharia coalfield was up to a depth of 1200m in April 2007. The total surface area of BCCL affected due to fire had been assessed to be 8.9 km^2 in 1995 against the earlier area of about17 km^2 at the time of nationalization. The quantum of coal burnt as per earlier assessment is 37 million tones and total reserves are about 17,077 million tonnes. According to the research work of (Chatterjee et al., 2007) various reclamation measures have been adopted by BCCL, Dhanbad for preventing coal fires from further propagation. Some of the mentioned techniques are surface blanketing by incombustible material, infusion of inert gas, hydraulic blind flushing through boreholes, etc.

3.2.2. Mining history of J.C.F and present scenario

Coal mining was started in J.C.F in the early 1890's. J.C.F was one of the best for mining because it had several thick coal seams which were at relatively shallow depths beneath the surface. It was proven that the falcate shaped basin of the coal field has approximately 1 billion tonnes of coal reserves (Singh, Jain, Paul, Gupta, & Raju, n.d.). Coal mining is performed by both open cast (OC) and under-ground (UG) methods. Coal is the primary source of energy in India. Mining in this coalfield was started 100 years ago approximately and is still continuing. Bharat coking coal limited (BCCL) is the primary mining agency in this area and it supplies about 40% of nation's coking coal.

3.3. Scientific significane of study area

Geologic formation of the coalfield and being primary coking coal reserve are not only the characteristics which define the uniqueness of this coalfield but also the mine fires, land degradation and also the environmental pollution. It is considered to be one of the world's most degraded coal field. Environmental problems and land degradation problems in this coal field are due to various factors such as

a) Mining activities,
b) Overburden dumps,
c) Abandoned quarries,
d) Ground water depletion
e) Degraded vegetation and
f) Coal fires.

Land subsidence and coal fires are major factors of land degradation in and around Jharia coal field (JCF). This coal field is much degraded and it exhibits severe environmental problems in land, air and water (Singh et al., n.d.). It is evident that different types of scatteres are found in this study area which are:

a) Permanent scatterers: Urban features such as buildings in and around Dhanbad city and other villages act as permanent scatterers.
b) Volume scatterers: The vegetation in this region acts as volume scatterers.

The water bodies like Katri river in the east and Damodar River in the south of the study area causes specular reflection to the RADAR signal. The terrain in this region is continuously changing with time due to mining activities. Interferometric pairs with low temporal baselines over this study area would be feasible to get accurate deformation measurements.
Dumping of the fire-affected portions of the affected coal seams and overburden dumps at a safe place to let burn out naturally and completely is one such coal fire reclamation practise. This place will also be detected as thermal anomaly in remotely sensed image.

4. DATASET USED

4.1. ASTER

ASTER is one of the five state-of-the-art instrument sensor systems on-board Terra a satellite launched in December 1999. It was built by a consortium of Japanese government, industry, and research groups. ASTER monitors cloud cover, glaciers, land temperature, land use, natural disasters, sea ice, snow cover and vegetation patterns at a spatial resolution of 90 to 15 meters.

Table 4-1: ASTER Satellite system: Sensor Characteristics

Launch Date	18 December 1999 at Vandenberg Air Force Base, California, USA
Equator Crossing	10:30 AM (north to south)
Orbit	705 km altitude, sun synchronous
Orbit Inclination	98.3 degrees from the equator
Orbit Period	98.88 minutes
Ground Track Repeat Cycle	16 days
Resolution	15 to 90 meters (depending on in spectral band)

The ASTER instrument consists of three separate instrument subsystems:

1. Visible Near Infrared (VNIR)
2. Short Wave Infrared (SWIR)
3. Thermal Infrared (TIR)

Table 4-2: ASTER Band Specifications

Instrument	VNIR	SWIR	TIR
Bands	1-3	4-9	10-14
Spatial Resolution	15m	30m	90m
Swath Width	60km	60km	60km
Cross Track Pointing	± 318km (± 24 deg)	± 116km (± 8.55 deg)	± 116km (± 8.55 deg)
Quantisation (bits)	8	8	12

4.1.1. ASTER band selection

Table 4-3: ASTER TIR Band Specifications

Bands	Bandpass (μm)	Effective Wavelength (μm)
10	8.125-8.475	8.291
11	8.475-8.825	8.634
12	8.925-9.275	9.075
13	10.25-10.95	10.657
14	10.95-11.65	11.318

The TIR bands of ASTER are closely associated in wavelength and their content is highly correlated. In order to highlight the differences between these highly correlated bands, rationing is necessary. But in this case it is not possible. Band 10 (the shortest wavelength TIR band) was selected for detection since due to its short wavelength is the most sensitive band for higher temperature anomalies.

- Level 1B product is used in the study, one of the standard products of ASTER.
- It is geo-referenced, radiometric and geometric corrected data.
- TIR of two different time periods was used which are 25 October 2006 and 27 November 2009.

4.2. ALOS PALSAR

ALOS (Advanced Land Observing Satellite) was successfully launched by JAXA (Japan Aerospace Exploration Agency) on 24th January, 2006. PALSAR (Phased Array type L-band Synthetic Aperture Radar) is the sensor which is carried by ALOS. It can operate at four primary modes with different polarizations and off-nadir angles:

a) High resolution single-polarization (FBS) mode,
b) High-resolution dual-polarization (FBD) mode,
c) Fully-polarimetric (PLR) mode, and
d) ScanSAR mode.

Table 4-4: PALSAR satellite system: Sensor Characteristics

Imaging Frequency	L Band at 1270 MHz
Orbit	Sun Synchronous
Mean Altitude	691.65 km
Inclination	34.3°.
Orbit Period	100 min or 14 times a day
Repeat Cycle	46-days

ALOS orbits at an altitude of 691.65 km (at the equator) with 46-days repeat cycle. The centre frequency of PALSAR is 1270 MHz, resulting in a wavelength of 23.62 cm and incidence angle 34.3°.

Table 4-5: ALOS PALSAR Data Specifications

S.No	**Orbit**	**Date of Pass**	**Mode**	**Polarization**	**Frame**	**Node**
1	05421	30/01/2007	FBS	HH	460	Ascending
2	10118	18/12/2007	FBS	HH	460	Ascending
3	10789	02/02/2008	FBS	HH	460	Ascending
4	11460	19/03/2008	FBS	HH	460	Ascending
5	15486	20/12/2008	FBS	HH	460	Ascending
6	20854	23/12/2009	FBS	HH	460	Ascending
7	21525	07/02/2010	FBS	HH	460	Ascending
8	26222	26/12/2010	FBS	HH	460	Ascending

4.3. Digital Elevation Model (DEM)

Merged SRTM (Shuttle Radar Topographic Mission) and CARTOSAT DEM (2006 and 2011) of 25m and 10m spatial resolution respectively are used in the study with projection UTM (Universal Transverse Mercator), zone 45N and datum WGS-84. The vertical accuracy is 8m and horizontal accuracy is 15m.

4.4. LISS 3 and CARTOSAT 2 pan sharpened image

Geocoded LISS 3 and CARTOSAT 2 pan sharpened image was is also used to remove the false alarms, such as anomalous pixels from urban and industrial heat sources, river etc.

5. METHODOLOGY

5.1. Methodology adopted in the study

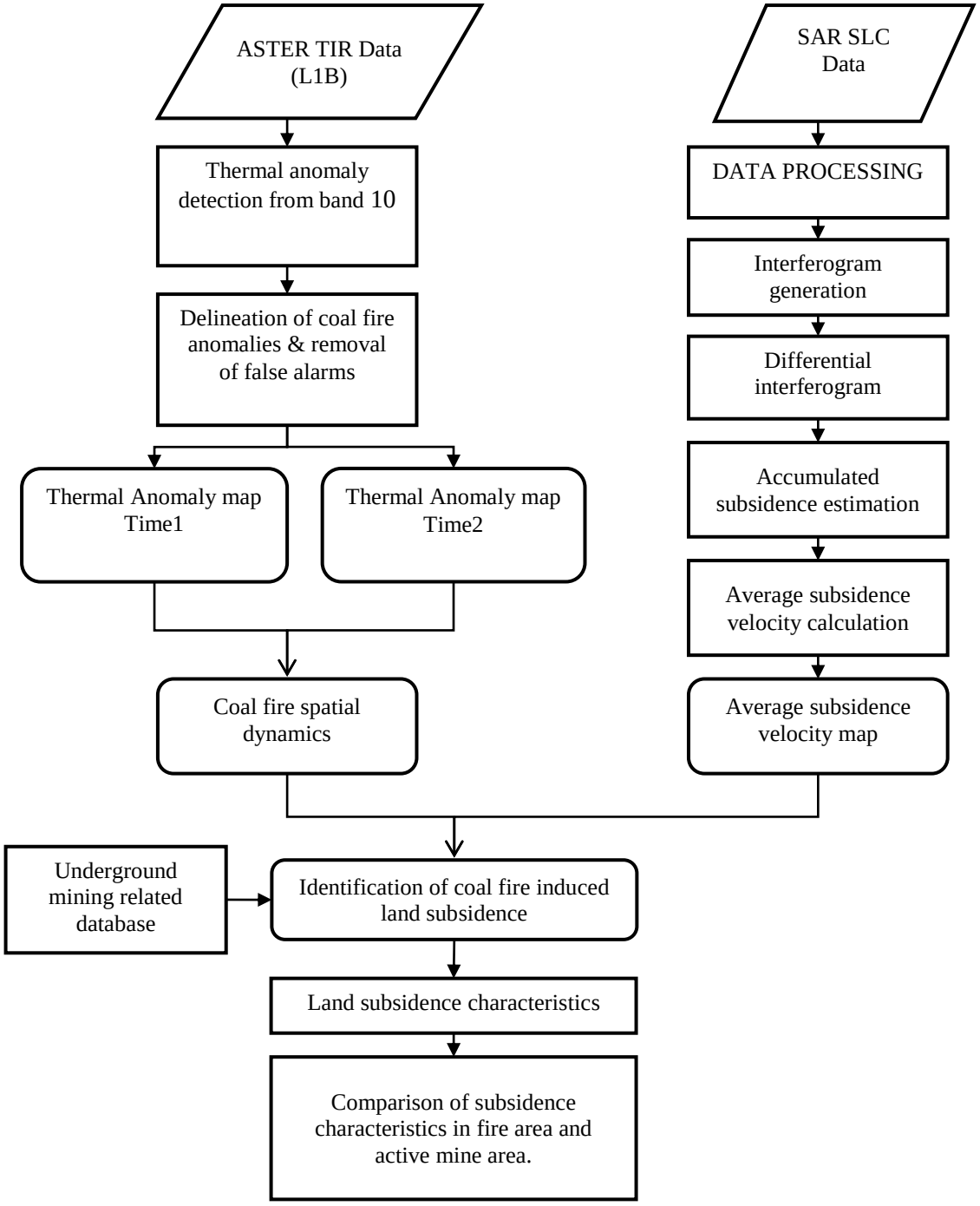

Figure 5-1: Flowchart of methodology

5.2. Algorithm: To detect coal fire anomalies

The following algorithm is based on the work of (C. Kuenzer et al., 2008), (J. Zhang, 2004) and (Hecker, Werff, & Bakker, 2011) used as implemented in IDL. This algorithm detects anomalously warm pixels based on comparison with background (i.e. neighbouring) pixels.

5.2.1. Automated moving window approach

In this approach a subset window of M1 columns and N1 rows is moved over an image having M number of rows and N number of columns (M1<=M and N1<=N). The window runs the anomaly test on all the pixels inside it.

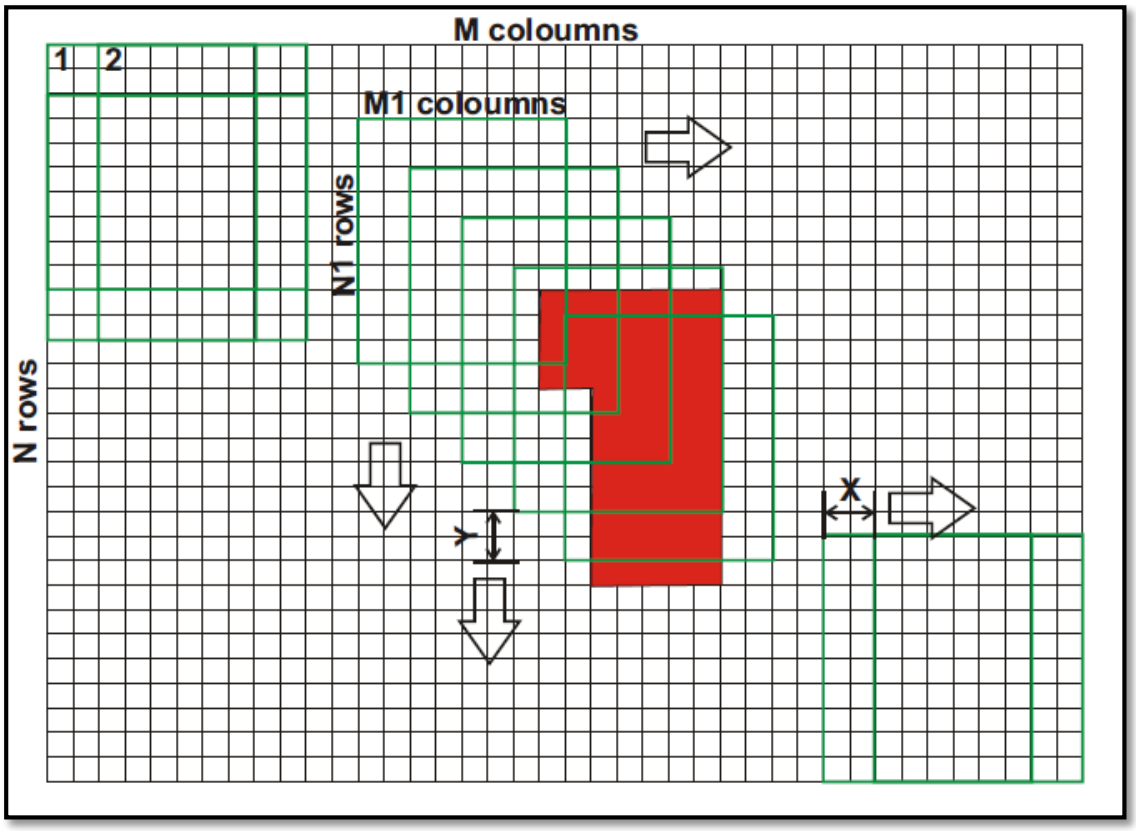

Figure 5-2: Moving window method, where subsets are divided through a moving window over it. Source (J. Zhang, 2004)

In figure (5-2), the window moves over the image with the step X (X<= M-M1) in the column direction and step Y (Y<= N-N1) in the row direction. The different kernels are in green and red blob indicates same coal fire area sampled several times with different kernel positions and kernel sizes.

The anomaly test: The histogram is calculated within the window every time it moves. To extract the thermal anomalies from the background pixels, threshold is applied. Threshold criterion classifies the image into binary image consisting of anomaly and the background. Threshold value is determined based on the statistics within each sub-segment of an image and the conditions to determine threshold value are mentioned below:

A primary condition: for the division between the anomalous pixels and background pixels is the first local minimum (or the first turning point) after the global maximum of the histogram.

A secondary condition: is that this point has to be at least at mean + standard deviation.

Moving window is decided by the user by setting parameters on kernel sizes to be analysed and by the increment the kernel is moved over the image. The kernel size parameters are explained in the next section.
Pixel is calculated many times in different subsets with all possible neighbourhood pixels. All pixels with values greater than the threshold point are considered anomalous. If there is no local minimum after the global maximum, no pixel is considered anomalous. However anomalous pixels in the image increase with the decrease in threshold values.
Window size (or kernel size): Depending on the spatial dimensions of coal fire, window size is decided to move over the image. In this case, window size is varied from 11*11 to 35 by 35. For each window size a result is kept in memory.

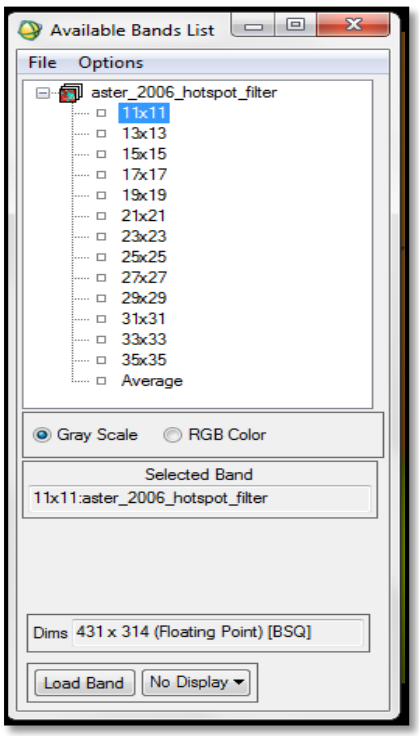

Figure 5-3: Saved output of different window sizes ranging from 11*11 to 35*35 and the normalized output of all the layers.

In each layer, the digital number of the saved output is equal to the number of times the pixel has been termed as thermally anomalous. For example, the DN holds a value 100 for a window size of 11*11that means, the pixel has been sampled 11*11= 121 times, out of which it has been termed as thermally anomalous 100 times.
The maximum value in the first layer is the 11*11= 121, similarly for second is 169 and for 13th layer is 1225. Each layer is normalized to the same maximum value as the 13th layer through its DN value times 1225 divided by the maximum value of the layer. After normalization, all the layers are summed up produce the 14th layer which represents the accumulation of the moving

window results. Its simulated threshold can be calculated as the mean of the 13 layers' threshold images.

Cut-off percentage: The number of times a pixel has been termed as anomalous, is visualised using cut-off percentage on the average 'layer 14'. The cut-off percentage strongly influence the output. Different results were observed with varying cut-off percenatges. With lower cut-off percentage, thermal anomalous pixels increases which results in higher number of false alarms.When the cut-off percentage is set low as 50%, there will be more number of thermal anomalous pixels extracted by the moving window. Also when it is set high such as 90%, there are less number of thermal anomalies in the output image. In this case, we have used cut-off percentage as 70%, which showed good reults in detecting coal fire related anomalies in China detected by (J. Zhang, 2004) and in Jharia by (C. Kuenzer et al., 2008).

Removing false alarms: Some false alarms, such as industrial sources and water bodies were also detected as thermally anomalous in comparsion to neighbouring pixels with this technique. Anomalies detected using cut-off percentage of 70% were overlaid on optical Pan sharpened image (Liss 3 and Cartosat 2) to remove the false alarms.

5.3. Validation of coal fires

The surface plans mapped using on-site field surveys in 2007-08 are used. A qualitative visual inspection of the coal fire anomalies detected using ASTER data were compared and validated with the surface plans.

5.4. Differential SAR interferometry

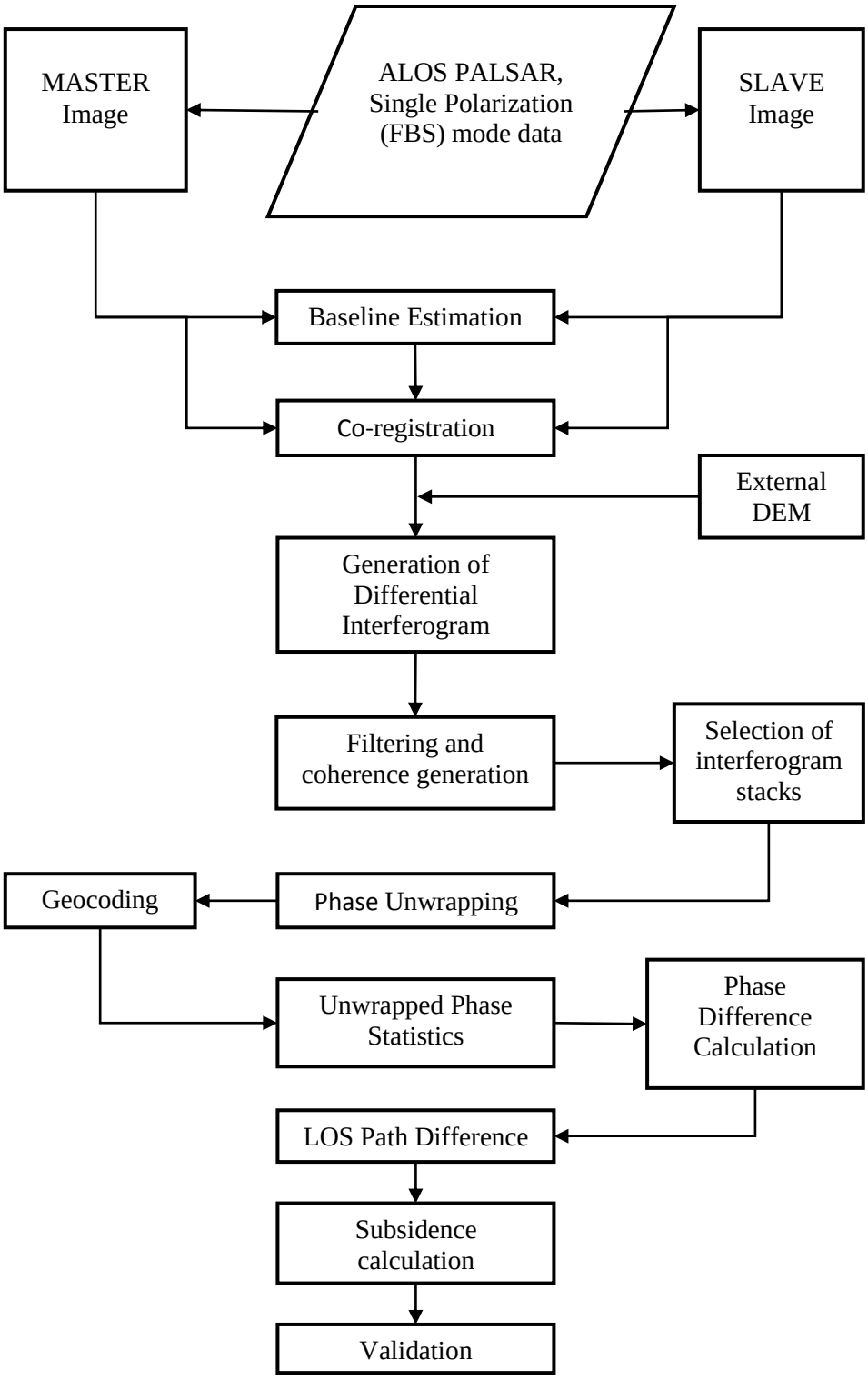

Figure 5-4: Flowchart of differential interferometry process

5.4.1. Multi-looking and co-registration

The raw files are imported into SARscape and converted into Single Look Complex (SLC) format. Master image and slave image is created by observing the date of pass. Multi-looking is performed for interpreting the actual boundary because it is difficult to interpret the features in this format. Subset of SLC images are utilized for baseline estimation and interferogram generation.

5.4.2. Baseline estimation

To obtain information about the baseline values and other orbital parameters related to the input pair, baseline estimation is carried out. When the ground reflectivity acquired with at least two antennae overlap interferogram generation is feasible ("Synthetic Aperture Radar and SARscape," 2009). When the perpendicular component of the baseline crosses further than a certain limit it is characterized as critical baseline. ("Synthetic Aperture Radar and SARscape," 2009). As a result of geometric de-correlation no phase information is preserved at this stage causing loss of coherence. The critical baseline is calculated as follows:

$$\mathrm{B_{n\sigma}} = \frac{\lambda R \tan\theta}{R_r} \tag{5-1}$$

where, Rr is the range resolution, and θ is the incidence angle

5.4.3. Interferogram generation

The SLC image is in the form of a two-dimensional array, wherein each pixel is associated with the phase and the amplitude. The amplitude is associated to surface reflectivity. The changes at the surface are associated with phase. Repeat pass acquisition is carried out in order to extract useful information from phase, for which a correlation between the phase terms can be deduced. Subtracting the two phases gives the height of the pixel in relation to the height of the sensor. Eventually, an interferogram is generated by multiplying one image by the complex conjugate of the other. The phase difference contributions from atmosphere, noise, topography and also any movement occurred during the master and slave acquisitions are incorporated in the generated interferogram. Hence, the interferogram generation is the process of pixel by pixel calculation of the Hermitian product of two co-registered SAR images.
The phase of an interferogram is calculated as follows:

$$\varphi = \tan^{-1}\left(\frac{Imag(I)}{Real(I)}\right) \tag{5-2}$$

where, $Imag(I)$ and $Real(I)$ are the imaginary and real parts of the interferogram
The interferogram pairs generated are displayed in appendix B.

5.4.4. Interferogram flattening and topographic phase removal

As a consequence of the InSAR imaging geometry, the interferogram generated in section (5.3) comprises of the flat earth effect. The flat earth effect is a consequence of the non-zero baseline. Because of the presence flat earth effect the points with the same height on the ground does not have the same interferometric phase (Y. Zhang, 2005). The Interferogram flattening is performed

to generate a residual interferogram which is free from topography. This process is carried out using a high quality external DEM as reference. The resultant interferogram contains fringes only related to displacements, change in elevation, noise and atmosphere. In this study two different external DEM were used. The details of the DEM are mentioned in section (4.3). Consequently, the generated differential interferograms comprises of the deformation fringes.

5.4.5. Filtering and coherence generation

The filtering process incorporates the reduction of noise in the interferogram. In an interferogram temporal de-correlation, baseline de-correlation and also thermal noise generated by the sensor are the sources of phase noise.

Coherence which is an indicator of phase quality is generated. The coherence calculated from two input co-registered SAR images ($S1$) and ($S1$) is defined as ("Synthetic Aperture Radar and SARscape," 2009):

$$\gamma = \frac{\sum|S_1(x).S_2(x)^*|}{\sqrt{\sum|S_1(x)|^2.\sum|S_2(x)|^2}} \quad (5\text{-}3)$$

The phase stability between the master-slave acquisitions is indicated by coherence. The coherence image values ranges between 0 and 1. The change in surface properties between acquisition will tends to zero causing the decrease of the coherence degree. So, a small change in the position and/or the physical characteristics of the surface scatterers within a given pixel is detected as low coherence (Abdelfattah & Nicolas, 2010).

The coherence is a function of complete spatial de-correlation and temporal de-correlation between master-slave acquisitions ("Synthetic Aperture Radar and SARscape," 2009). In general, coherence is inversely proportional to temporal baseline between master and slave image. Longer the time interval between master-slave acquisitions lower is the coherence. Phase related measurements are not derived interferogram pairs with low coherence.

The reliable surface information is present in the phase of the interferogram. Therefore, phase noise filtering is considered as an essential process to reduce the phase noise(Chao, Chen, & Lee, 2013).

In view of the fact that Boxcar filter operates well for homogeneous areas (Chao et al., 2013), it was used to detect the subsidence fringes.

The output of filtering and coherence is displayed in appendix C.

5.4.6. Phase unwrapping

The phase increases gradually as the terrain height increases. The interferometric phase values are of 2π cyclic nature. After reaching 2π the phase values get wrapped automatically. Deleting any integer number equivalent to an integer number of 2π phase cycles, the flattened interferogram provides a measurement of the actual altitude variation. The process of adding the correct integer multiple of 2π to the interferometric fringes is called phase unwrapping (Fletcher, European Space Agency, European Space Research and Technology Centre, & ESTEC, 2007).

5.4.7. Line of sight (LOS) path difference

$$\Delta\phi = \frac{2\pi}{\lambda} 2\Delta\rho \quad (5\text{-}4)$$

$$\Delta\rho = \frac{\Delta\phi\lambda}{4\pi} \quad (5\text{-}5)$$

where,

$\Delta\phi$ = the phase difference between the subsidence fringe and the background

$\Delta\rho$ = LOS path difference

λ = wavelength of the radar pulse

In case of ALOS PALSAR λ=23.62 cm

5.4.8. Subsidence

The subsidence measurements derived from the LOS path difference are calculated as follows:

$$\text{Subsidence} = \Delta\rho * \frac{1}{\cos 38^\circ} \quad (5\text{-}6)$$

where, cos 38°=0.95

5.4.9. Validation of land subsidence areas

Land subsidence due to underground mining is monitored by the agencies working in the coal field. The results were validated with the data provided by the agencies. The mining period of Jamadoba 6&7 mining site was from April 2006 to December 2007 and the rate of subsidence was 7.9 cm/ year. According to DInSAR observations, the subsidence rate was found to 8.74 cm per year. However, validation of coal fire induced land subsidence could not be conducted in the coal fire zones, because as such no data was available.

5.5. Detection of coal fire induced land subsidence

Coal fire induced land subsidence areas were detected by overlapping the results of thermal anomaly map (union of 2006 and 2009) over the DInSAR derived land subsidence map calculated between 2007 and 2010.

6. RESULTS AND DISCUSSION

This chapter describe the research outcomes from the procured data and discussion of the results.

6.1. Detection of coal fire affected areas and their spato-temporal dynamics

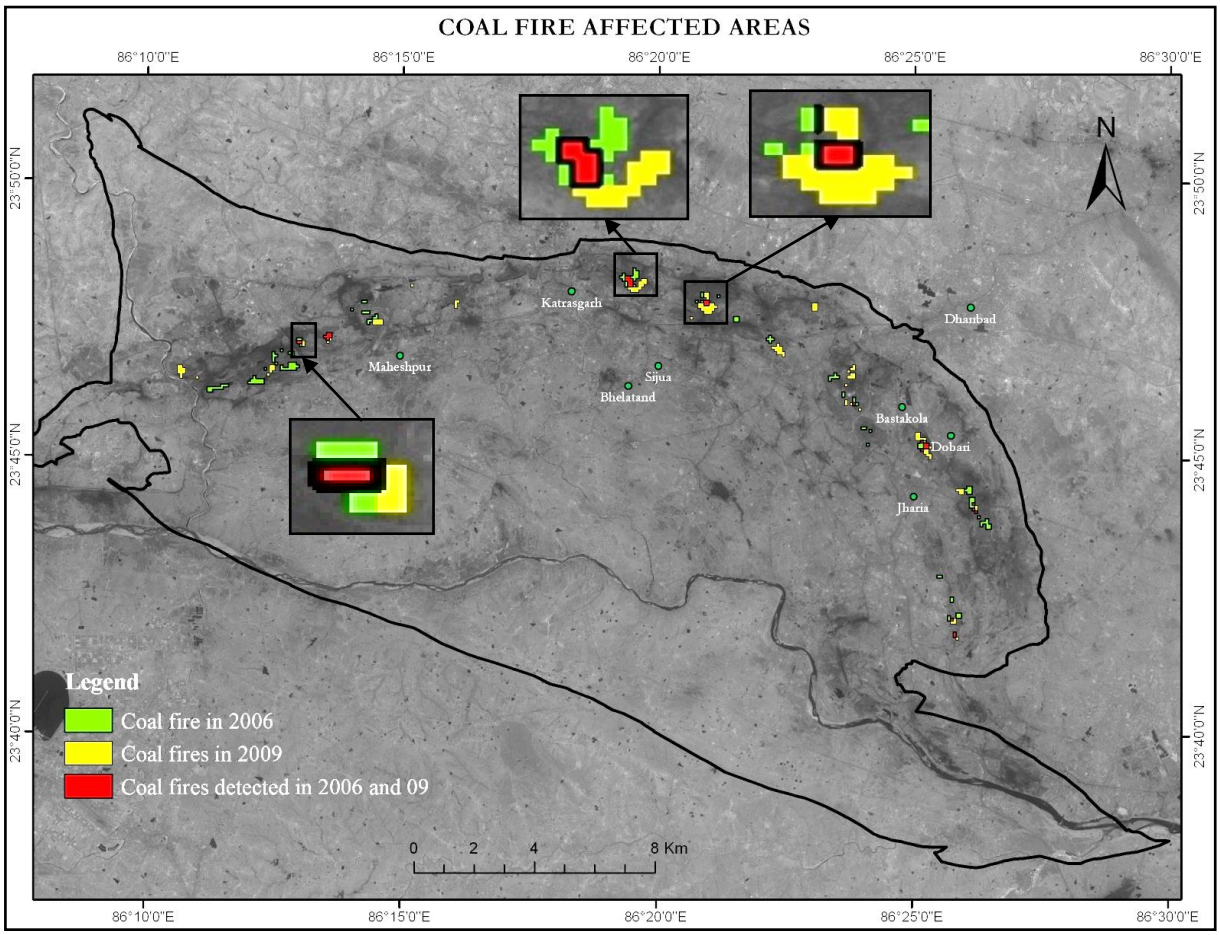

Figure 6-1: Coal fire affected areas in Jharia coalfield

In the year 2006, minimum spatial coverage of coal-fires was found to be 0.007 Km^2 near Maheshpur and maximum was found 0.20 Km^2 in the eastward direction of Katrasgarh. Minimum spatial coverage of coal-fires in the year 2009 was found 0.02 Km^2 near Bastakola and maximum was found to be 0.08 Km^2 near Jogta.

The areas marked in red highlights the areas with consistent fires detected in 2006 as well as in 2009. Some new fires have also been detected in some areas in the year 2009. Consistent coal fire zones are observed near Dobari, Katrasgarh, Jharia, Maheshpur. Coal fire dynamics for two

observation periods in the figure (6-3) indicates decrease from 1.46 Km^2 to 1.35 Km^2 in 2006 and 2009 respectively.

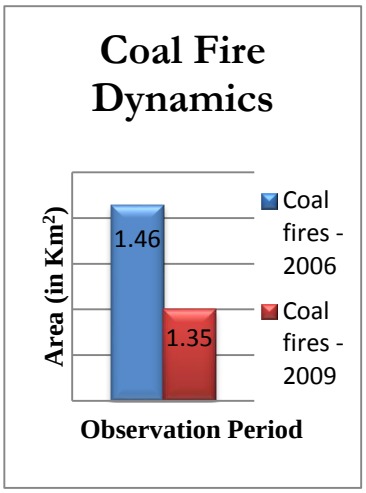

Figure 6-2: Coal fire dynamics.

The decrease in the spatial extent of coal fire areas is possible due to fire reclamation efforts carried out by the mining agencies (discussed in section 3.2.1). It is also possible that some fires can be mature enough to increase the temperature of the coal fire zone to be detected as thermally anomalous pixel in a satellite image. General direction of movement of fire in aster images is towards east.While investigating the coal fire dynamics, factors such as wind direction, wind speed, dip directions of the coal seam and air temperature are not considered in the present study. More likely dip directions of the coal seams would make burning of the fires in an up dip direction.

6.2. Detection of coal fire induced land subsidence areas

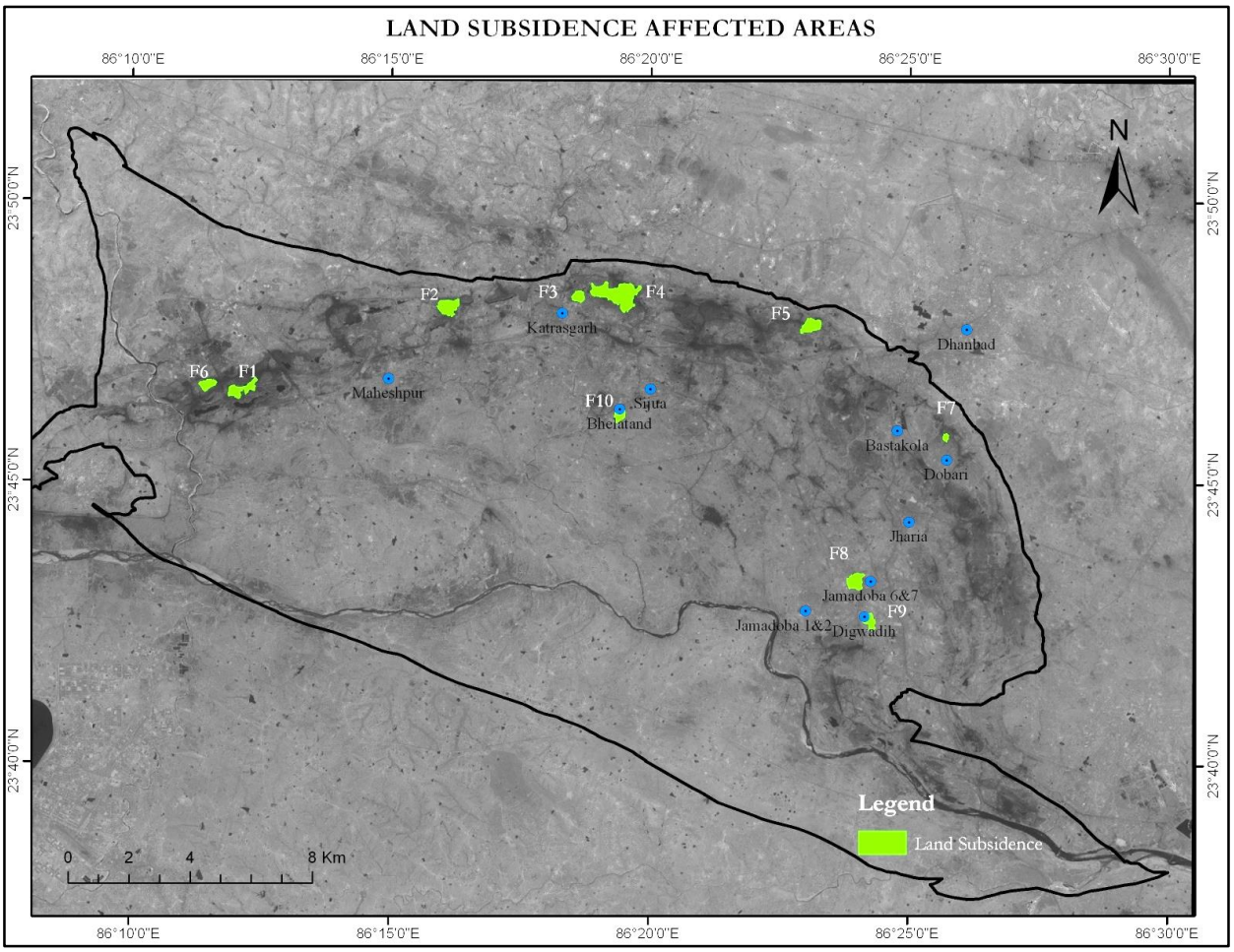

Figure 6-3: Land subsidence affected area detected using DInSAR.

Observations in figure (6-3) indicates land subsidence phenomena in the coalfield by DInSAR processing. According to the database provided by agencies, subsidence near Bhelatand (fringe id F6), Jamadoba 6&7 (fringe id F8) and Digwadih (fringe id F9) is due to ongoing active underground coal mining.

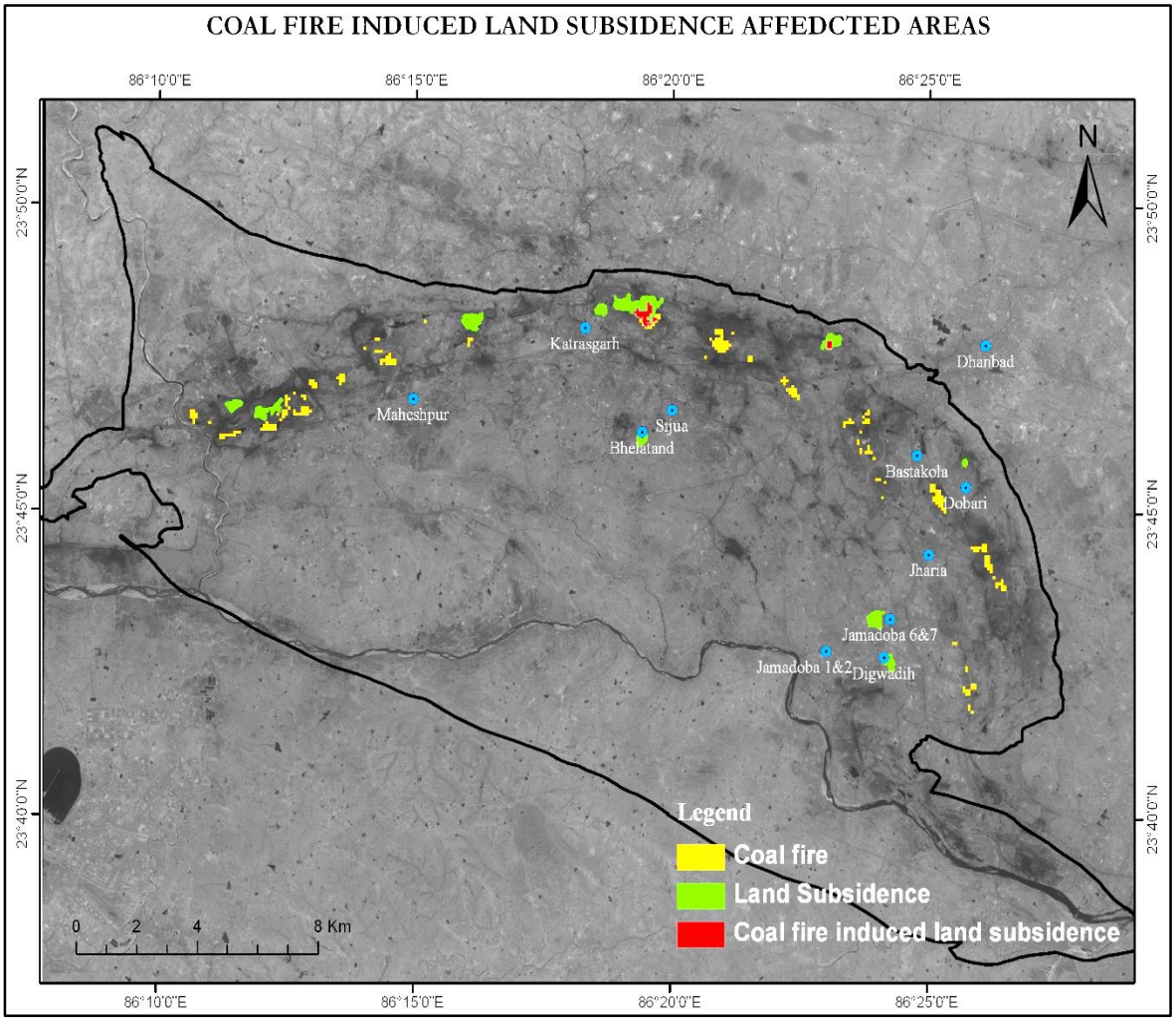

Figure 6-4: Coal fire induced land subsidence affected areas.

From the integrated approach we are able to recognize coal fire related land subsidence by overlapping the thermal anomalies with the DInSAR derived land subsidence results. Coal fire induced land subsidence was detected in the north of Jharia coalfield. However, so far no comparison with direct field measurements of subsidence rates induced by coal fires could not be conducted.

6.3. Investigation of the characteristics of coal fire induced land subsidence in comparison to coal mining induced land subsidence.

6.3.1. Spatial dynamics of subsidence areas

The overlapping subsidence fringes observed in the DInSAR processing were used to monitor the subsidence phenomenon. The subsidence fringes which overlapped with the coal fire zones having fringe ID (F4 and F5). The details of the fringe statistics are discussed in Appendix-E. The subsidence zones having fringe IDs F2 and F6 mentioned in figure (6-3) do not overlap with the coal fire areas.

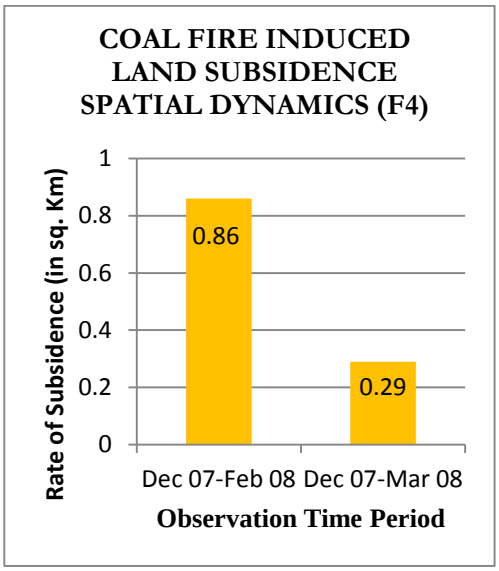

Figure 6-5: Coal fire induced land subsidence spatial dynamics (F4)

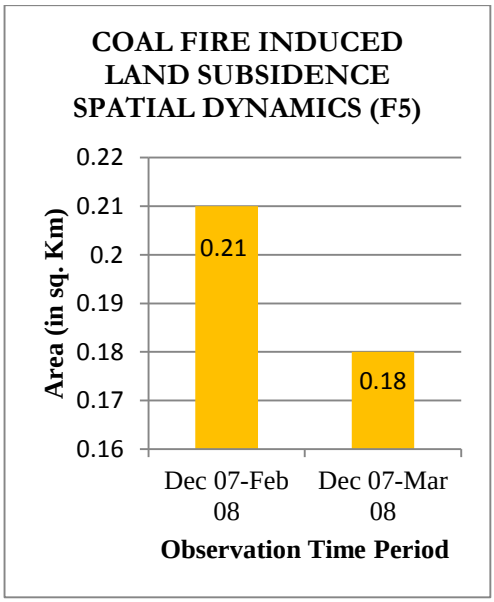

Figure 6-6: Coal fire induced land subsidence spatial dynamics (F5)

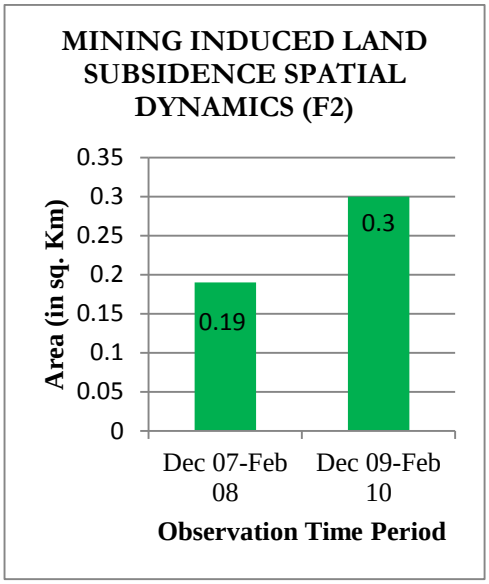

Figure 6-7: Mining induced land subsidence spatial dynamics (F2)

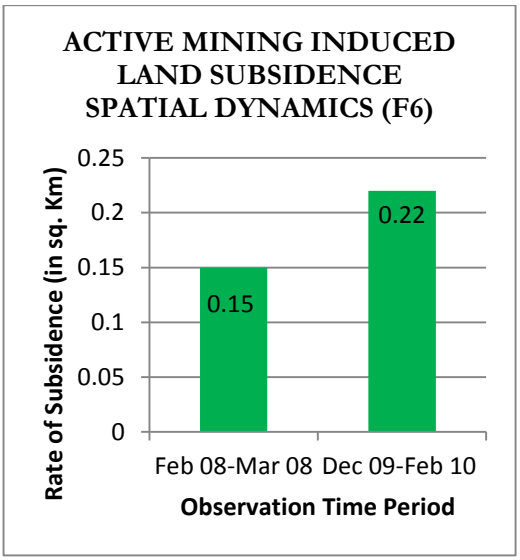

Figure 6-8: Active mining induced land subsidence spatial dynamics (F10)

The spatial extent of coal fire related land subsidence affected areas was found to decrease with passage of time in figure (6-5) and figure (6-6). As some of the fires would be mature enough to cause subsidence. However in case of the spatial coverage of mining induced subsidence areas is increased. The affected areas increase with the subsidence phenomena caused by ongoing underground mining activities. The mined areas are not provided the pillar support completely.

6.4. To test if the temporal development of two subsidence types are significantly differ from each other in DInSAR processing alone.

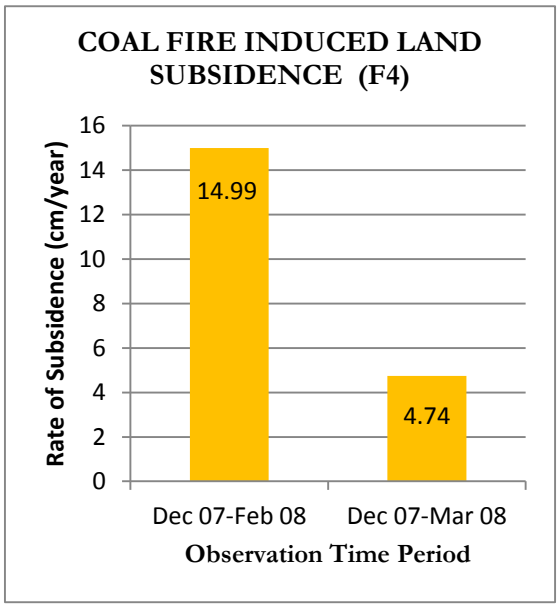

Figure 6-9: Coal fire induced land subsidence observed using DInSAR for (F4)

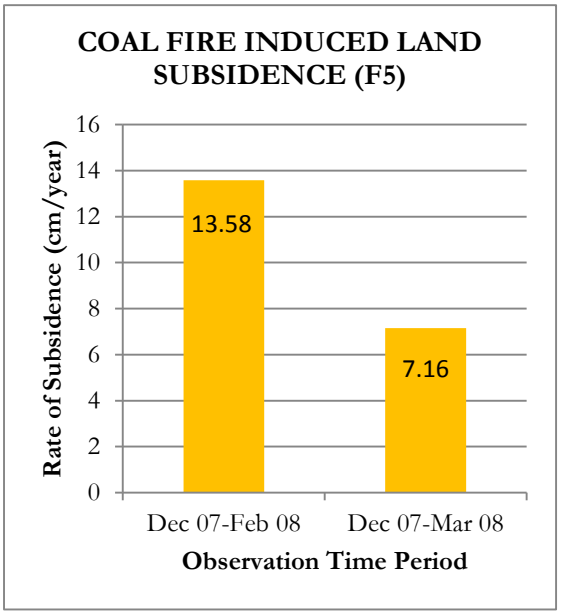

Figure 6-10: Coal fire induced land subsidence observed using DInSAR for (F5)

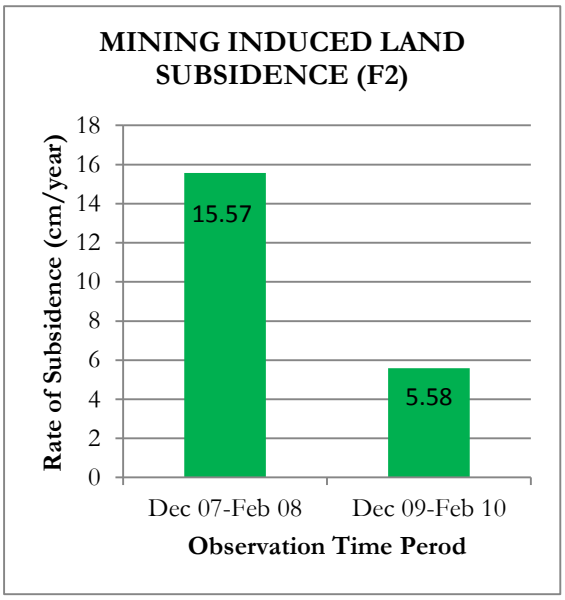

Figure 6-11: Mining induced land subsidence observed using DInSAR for (F2)

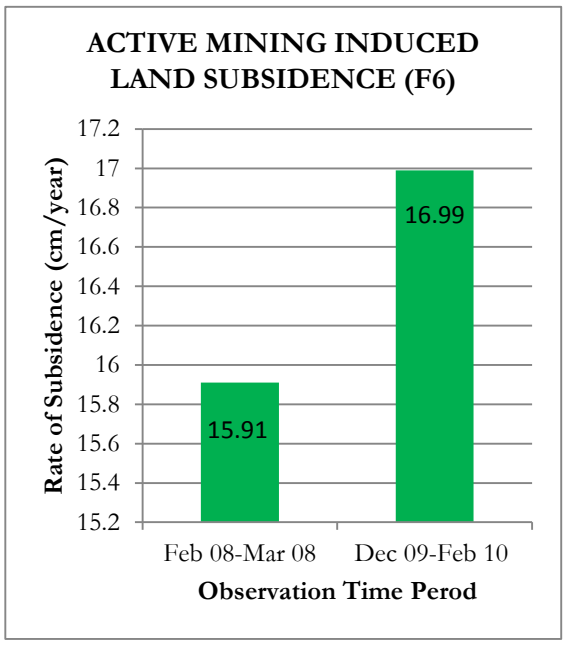

Figure 6-12: Active Mining induced land subsidence observed using DInSAR for (F10)

From the DInSAR processing, out of 28 intererogram pairs generated, only four interferogram pairs revealed informative fringes. These interferogram pairs have better coherence than other pairs. Loss of coherence could be the reason for the loss of information. The detailed information about the interferogram pairs is mentioned in the appendix A.

The time series of the subsidence rates could not be generated due to limited number of repetitive fringes inside a subsidence zone. However, with these limited number of repetitive fringes, coal fire induced land subsidence areas shows decrease in the rate of subsidence with the

passage of time. The mining induced subsidence phenomena shows gradual increase in subsidence rates at active mining site and decrease at another at other mining site.

7. CONCLUSION AND RECOMMENDATIONS

7.1. Conclusions

The spatial dynamics of coal fire observed helped to know the fire propagation direction. The DInSAR processed results demonstrated its capability of mapping and monitoring land deformations. Combining the results of coal fire related anomalies and land subsidence areas facilitated to detect and analyse coal fire induced land subsidence. The findings of the research carried out helped in answering the following questions.

1. **How well can we map thermal anomalies with ASTER data?**

A qualitative visual inspection indicates that the thermal anomalies agree well with the coal fire maps derived from on-site field surveys. According the surface plans the total area covered by coal fire zones is 16.48 Km^2 of the total study area. However, the ASTER data derived coal fires showed spatial coverage of coal fires 1.45 Km^2 and 1.36 Km^2 in the year 2006 and 2009 respectively.

In general coal fire is a very local phenomenon. In many cases, cracks and voids of few meters are not hot enough to saturate a pixel of 90 meters to be considered as thermal anomaly in comparison to background. The cumulative temperature of the pixel depends on location, surface type, spread, and temperature of fire/crack and its surroundings. The detection capability of a dataset for coal-fire-induced thermal anomalies is dependent on the image spatial resolution, the temperature and size of a thermal anomaly, and also the temperature contrast between a thermal anomaly and the background. It is subject of further investigation to detect and monitor coal fires considering the above the mentioned factors.

2. **How well do the deformations observed coincide with the coal fire?**

The observations showed satisfactory results where the deformations showed good coincidence with the coal fires. Not all the coal fire areas developed subsidence. The outcomes of the study demonstrated that the integrated analysis of combing thermal anomalies with DInSAR results to differentiate the land subsidence effects related to coal fire from those related to other subsidence sources. So far no comparison with direct field measurements of subsidence rates induced by coal fires could not be conducted.

3. **Do all the coal fires detected show subsidence? What is the contribution of coal fire induced land subsidence to overall subsidence scenario?**

According to the observations, not only the coal fires are the reason for subsidence. Coal mining carried out in the coalfield is also one of the reason of land subsidence. The overall subsidence scenario observed using DInSAR data processing approach during a period of 2007-2010 is 3.14 Km^2. Out which 1.07 Km^2 area is affected by land subsidence due to coal fires which approximate 34% of the total subsidence phenomena.

4. **What is the nature of subsidence, gradual or sudden?**

As discussed in the previous section (6.4) due to limited number of repetitive subsidence fringes in subsidence affected zones, the time series of the subsidence rate could not be generated. So far

with the results obtained from DInSAR processing, the nature of subsidence due to coal fires is observed to be gradual.

5. **How the spatial extent and rate of subsidence vary in relation to spatio-temporal dynamics of coal fire?**

The coal fire induced subsidence phenomena was observed only at two different locations in the coal field. From the spatial dynamics of coal fire and the land subsidence observations, it was perceived that the spatial extent of subsidence phenomena was moving in the same direction as the coal fire.

6. **How the spatio-temporal dynamics of coal fire induced land subsidence differ from mining induced land subsidence?**

The spatio-temporal characteristics of coal fire induced land subsidence shows that the spatial coverage of affected areas is decreased on the other hand the spatial extent of mining induced subsidence affected areas increased with the passage of time.

The assessment of coal fires using differential radar interferometry still has to be further developed in order to serve as reliable analysis and monitoring tool.

7. **What is the influence of subsidence on the development of coal fire and what are the possible governing factors?**

Ignition of underground coal fires is a slow process. Generally, cracks developed due to land subsidence serves as inlets for oxygen to ignite underground coal fire spread. In present research, coal fire pixels were observed in 2009 on the earlier developed land subsidence zone.

7.2. Recommendations

- To better understand the coal fire dynamics, it is recommended to consider factors such as wind direction, wind speed, dip angle, air temperature of the study area.
- Also the dynamics of coal fire are studied only for two years in the present research, it recommended to investigate the dynamics with higher number of observation period.
- It is also recommended for future studies to measure field based subsidence rates in the coal fire zones and establish their quantitative comparisons.

REFERENCES

Abdelfattah, R., & Nicolas, J.-M. (2010). Mixture model for the segmentation of the InSAR coherence map. *International Journal of Applied Earth Observation and Geoinformation*, *12*, S138–S144. doi:10.1016/j.jag.2009.10.001

Brady, B. H. G., & Brown, E. T. (2006). Mining-induced surface subsidence. In *Rock Mechanics for underground mining* (pp. 484–517). Springer.

Chao, C.-F., Chen, K.-S., & Lee, J.-S. (2013). Refined Filtering of Interferometric Phase From InSAR Data. *IEEE Transactions on Geoscience and Remote Sensing*, *51*(12), 5315–5323. doi:10.1109/TGRS.2012.2234467

Chatterjee, R. S. (2006). Coal fire mapping from satellite thermal IR data – A case example in Jharia Coalfield, Jharkhand, India. *ISPRS Journal of Photogrammetry and Remote Sensing*, *60*(2), 113–128. doi:10.1016/j.isprsjprs.2005.12.002

Chatterjee, R. S., Wahiduzzaman, M., Shah, A., Raju, E. V. R., Lakhera, R. C., & Dadhwal, V. K. (2007). Dynamics of coal fire in Jharia Coalfield, Jharkhand, India during the 1990s as observed from space. *CURRENT SCIENCE-BANGALORE-*, *92*(1), 61.

Dong, S., Yin, H., Yao, S., & Zhang, F. (2013). Detecting surface subsidence in coal mining area based on DInSAR technique. *Journal of Earth Science*, *24*(3), 449–456. doi:10.1007/s12583-013-0342-1

Ellyett, C. D., & Fleming, A. W. (1974). Thermal infrared imagery of the Burning Mountain coal fire. *Remote Sensing of Environment*, *3*(1), 79–86.

Fan, H., Deng, K., Ju, C., Zhu, C., & Xue, J. (2011). Land subsidence monitoring by D-InSAR technique. *Mining Science and Technology (China)*, *21*(6), 869–872. doi:10.1016/j.mstc.2011.05.030

Fletcher, K., European Space Agency, European Space Research and Technology Centre, & ESTEC. (2007). *InSAR principles: guidelines for SAR interferometry processing and interpretation*. Noordwijk, the Netherlands: ESA Publications Division, ESTEC.

Gabriel, A. K., Goldstein, R. M., & Zebker, H. A. (1989). Mapping small elevation changes over large areas: Differential radar interferometry. *Journal of Geophysical Research: Solid Earth (1978–2012)*, *94*(B7), 9183–9191.

Gangopadhyay, P. K., Maathuis, B., & Van Dijk, P. (2005). ASTER-derived emissivity and coal-fire related surface temperature anomaly: a case study in Wuda, north China. *International Journal of Remote Sensing*, *26*(24), 5555–5571. doi:10.1080/01431160500291959

Gupta, M., Mohanty, K. K., Kumar, D., & Banerjee, R. (2013). Monitoring surface elevation changes in Jharia coalfield, India using synthetic aperture radar interferometry. *Environmental Earth Sciences*. doi:10.1007/s12665-013-2664-9

Hecker, C., Werff, D. H. van der, & Bakker, W. (2011). *Pilot Study on Detection of Industrial Heat Sources by Remote Sensing*. ITC Faculty of Geo-Information Science and Earth Observation, University of Twente.

Jiang, L., Lin, H., Ma, J., Kong, B., & Wang, Y. (2011). Potential of small-baseline SAR interferometry for monitoring land subsidence related to underground coal fires: Wuda (Northern China) case study. *Remote Sensing of Environment*, *115*(2), 257–268. doi:10.1016/j.rse.2010.08.008

Kuenzer, C., & Dech, S. (2013). Theoretical Background of Thermal Infrared Remote Sensing. In C. Kuenzer & S. Dech (Eds.), *Thermal Infrared Remote Sensing* (Vol. 17, pp. 1–26). Dordrecht: Springer Netherlands.

Kuenzer, C., Hecker, C., Zhang, J., Wessling, S., & Wagner, W. (2008). The potential of multidiurnal MODIS thermal band data for coal fire detection. *International Journal of Remote Sensing*, *29*(3), 923–944. doi:10.1080/01431160701352147

Li, F. K., & Goldstein, R. M. (1990). Studies of multibaseline spaceborne interferometric synthetic aperture radars. *Geoscience and Remote Sensing, IEEE Transactions on*, *28*(1), 88–97.

Motagh, M., Walter, T. R., Sharifi, M. A., Fielding, E., Schenk, A., Anderssohn, J., & Zschau, J. (2008). Land subsidence in Iran caused by widespread water reservoir overexploitation. *Geophysical Research Letters*, *35*(16). doi:10.1029/2008GL033814

Prakash, A., Fielding, E. J., Gens, R., Van Genderen, J. L., & Evans, D. L. (2001). Data fusion for investigating land subsidence and coal fire hazards in a coal mining area. *International Journal of Remote Sensing*, *22*(6), 921–932. doi:10.1080/014311601300074441

Singh, G., Jain, M. K., Paul, B., Gupta, R. D., & Raju, E. V. (n.d.). Clusterization of mines for obtaining comprehensive environmental clearance: A case study of BCCL lease hold areas. *Journal of Indian School of Mines*, *Special Volume 2010*, 13–20.

Synthetic Aperture Radar and SARscape. (2009, August). sarmap.

Tomás, R., Romero, R., Mulas, J., Marturià, J. J., Mallorquí, J. J., Lopez-Sanchez, J. M., … Blanco, P. (2013). Radar interferometry techniques for the study of ground subsidence phenomena: a review of practical issues through cases in Spain. *Environmental Earth Sciences*. doi:10.1007/s12665-013-2422-z

Voigt, S., Tetzlaff, A., Zhang, J., Künzer, C., Zhukov, B., Strunz, G., Mehl, H. (2004). Integrating satellite remote sensing techniques for detection and analysis of uncontrolled coal seam fires in North China. *International Journal of Coal Geology*, *59*(1-2), 121–136. doi:10.1016/j.coal.2003.12.013

Yang, C., Zhang, Q., Zhao, C., Ji, L., & Zhu, W. (2010). Monitoring mine collapse by D-InSAR. *Mining Science and Technology (China)*, *20*(5), 696–700. doi:10.1016/S1674-5264(09)60265-9

Zebker, H. A., Rosen, P. A., Goldstein, R. M., Gabriel, A., & Werner, C. L. (1994). On the derivation of coseismic displacement fields using differential radar interferometry: The Landers earthquake. *Journal of Geophysical Research*, *99*(B10), 19617. doi:10.1029/94JB01179

Zeitoun, D. G., & Wakshal, E. (2013). *Land subsidence analysis in urban areas the Bangkok Metropolitan area case study*. Dordrecht: Springer.

Zhang, J. (2004, April 1). *Spatial and statistical analysis of thermal satellite imagery for extraction of coal fire related anomalies* (Phd Thesis). Vienna University of Technology, Vienna, Austria.

Zhang, Y. (2005). A comparison of the different models used for interferograms flattening. In *Geoscience and Remote Sensing Symposium, 2005. IGARSS'05. Proceedings. 2005 IEEE International* (Vol.8,pp. 5494–5496).IEEE.

Zhou, L., Zhang, D., Wang, J., Huang, Z., & Pan, D. (2013). Mapping Land Subsidence Related to Underground Coal Fires in the Wuda Coalfield (Northern China) Using a Small Stack of ALOS PALSAR Differential Interferograms. *Remote Sensing*, *5*(3), 1152–1176. doi:10.3390/rs5031152

APPENDIX-A

Details of interferogram pairs

Table A-1: Details of interferogram pairs

S. No	MASTER ORBIT-SLAVE ORBIT	DAY OF PASS		BASELINE			2 Pi AMBIGUITY	DOPPLER	RANGE SHIFT (pixels)	AZIMUTH SHIFT (pixels)	SEASON	COHERENCE	
		MASTER SCENE	SLAVE SCENE	NORMAL (m)	CRITICAL (m)	TEMPORAL (DAYS)	HEIGHT (m)	CENTROID DIFFERENCE (CRITICAL=2159.827 Hz)				Mean	Std. Dev
1	5421-10118	1/30/2007	12/18/2007	1320.308	13112.631	322	48.668	-8.651	-2038.036	-397.073	Jan-Dec	0.155	0.077
2	5421-10789	1/30/2007	2/2/2008	1851.591	13111.783	368	34.702	-11.102	-27.877	94.138	Jan-Feb	0.157	0.087
3	5421-11460	1/30/2007	3/19/2008	1676.413	13111.783	414	38.328	-16.057	-42.846	117.516	Jan-Mar	0.15	0.844
4	5421-15486	1/30/2007	12/20/2008	809.634	13111.783	690	79.361	0.224	-45.257	100.818	Jan-Dec	0.125	0.071
5	5421-20854	1/30/2007	12/23/2009	784.466	13111.783	1058	81.907	9.508	-49.098	2159.827	Jan-Dec	0.107	0.069
6	5421-21525	1/30/2007	2/7/2010	1160.089	13111.783	1104	55.387	-7.373	-28.39	133.013	Jan-Feb	0.112	0.071
7	5421-26222	1/30/2007	12/26/2010	1994.59	13111.783	1426	32.214	-0.187	-41.107	103.647	Jan-Dec	0.094	0.055
8	10118-10789	12/18/2007	2/2/2008	534.579	13027.664	46	119.598	-2.245	1939.352	384.175	Dec-Feb	0.55	0.181
9	10118-11460	12/18/2007	3/19/2008	356.375	13027.664	92	179.403	-7.2	1934.364	387.093	Dec-Mar	0.364	0.144
10	10118-15486	12/18/2007	12/20/2008	2126.318	13027.664	368	30.068	9.081	1933.764	385.283	Dec-Dec	0.146	0.085
11	10118-20854	12/18/2007	12/23/2009	582.232	13027.664	736	109.809	18.365	1932.362	384.368	Dec-Dec	0.123	0.8

S. No	MASTER ORBIT-SLAVE ORBIT	DAY OF PASS		BASELINE			2 Pi AMBIGUITY	DOPPLER	RANGE SHIFT (pixels)	AZIMUTH SHIFT (pixels)	SEASON	COHERENCE	
		MASTER SCENE	SLAVE SCENE	NORMAL (m)	CRITICAL (m)	TEMPORAL (DAYS)	HEIGHT (m)	CENTROID DIFFERENCE (CRITICAL=2159.827 Hz)				Mean	Std. Dev
12	10118-21525	12/18/2007	2/7/2010	170.157	13027.664	782	375.739	1.484	1939.234	389.288	Dec-Feb	0.127	0.764
13	10118-26222	12/18/2007	12/26/2010	703.195	13027.664	1104	90.92	8.67	1934.918	386.841	Dec-Dec	0.103	0.104
14	10789-11460	2/2/2008	3/19/2008	182.358	13006.259	46	350.148	-4.955	-14.968	25.344	Feb-Mar	0.44	0.148
15	10789-15486	2/2/2008	12/20/2008	2656.016	13006.259	322	24.041	11.326	-16.749	8.866	Feb-Dec	0.146	0.083
16	10789-20854	2/2/2008	12/23/2009	1113.121	13006.259	690	57.363	20.61	-20.964	-0.452	Feb-Dec	0.125	0.078
17	10789-21525	2/2/2008	2/7/2010	693.754	13006.259	736	92.039	3.729	-0.352	40.905	Feb-Feb	0.126	0.08
18	10789-26222	2/2/2008	12/26/2010	322.237	13006.259	1058	198.153	10.915	-13.292	11.329	Feb-Dec	0.11	0.072
19	11460-15486	3/19/2008	12/20/2008	2482.9	13010.393	276	25.724	16.282	-1.739	-16.454	Mar-Dec	0.139	0.08
20	11460-20854	3/19/2008	12/23/2009	931.125	13010.393	644	68.595	25.565	-5.981	-25.802	Mar-Dec	0.121	0.075
21	11460-21525	3/19/2008	2/7/2010	522.205	13010.393	690	122.309	8.684	14.623	15.568	Mar-Feb	0.128	0.08
22	11460-26222	3/19/2008	12/26/2010	389.839	13010.393	1012	163.838	15.87	1.669	-12.034	Mar-Dec	0.107	0.069
23	15486-20854	12/20/2008	12/23/2009	1591.944	13102.934	368	40.34	9.283	-4.252	-7.351	Dec-Dec	0.166	0.093
24	15486-21525	12/20/2008	2/7/2010	1959.582	13102.934	414	32.772	-7.597	16.353	32.02	Dec-Feb	0.167	0.091
25	15486-26222	12/20/2008	12/26/2010	2802.422	13102.934	736	22916	-0.412	3.393	4.415	Dec-Dec	0.114	0.066
26	20854-21525	12/23/2009	2/7/2010	461.416	13043.168	46	138.416	-16.881	20.6	41.374	Dec-Feb	0.5	0.15
27	20854-26222	12/23/2009	12/26/2010	1218.468	13043.168	368	52.519	-9.695	7.633	13.763	Dec-Dec	0.5	0.15
28	21525-26222	2/7/2010	12/26/2010	872.617	13033.501	322	73.294	7.186	-12.934	-27.578	Feb-Dec	0.182	0.104

APPENDIX-B

Coherence images of interferogram pairs

Figure B-1: Interferogram pair (10118-10789)

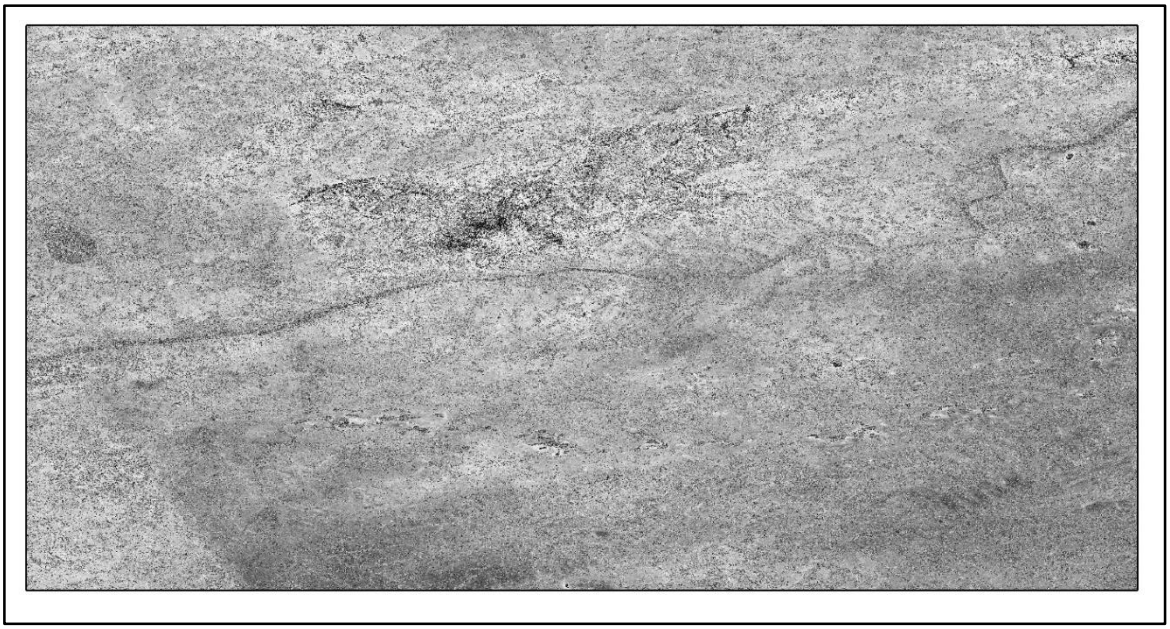

Figure B-2: Interferogram pair (10118-11460)

Figure B-3: Interferogram pair (10789-11460)

Figure B-4: Interferogram pair (20854-21525)

APPENDIX-C

Filtered output of interferogram fringes

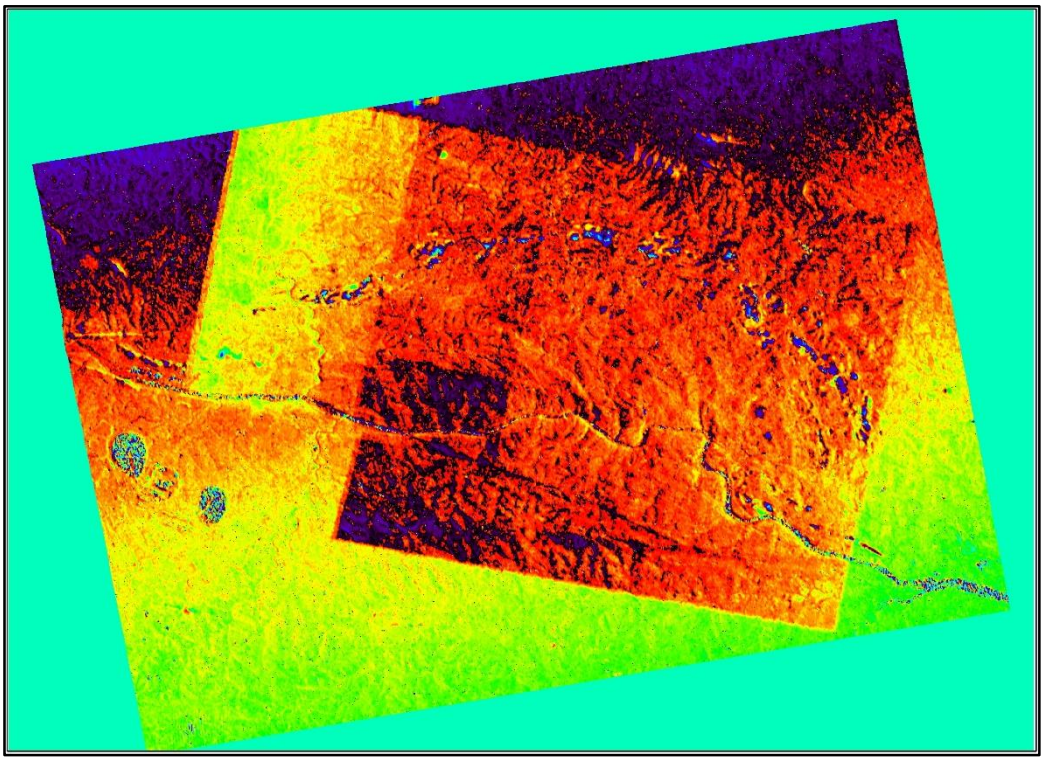

Figure C-1: Filtered image pair (10118-10789)

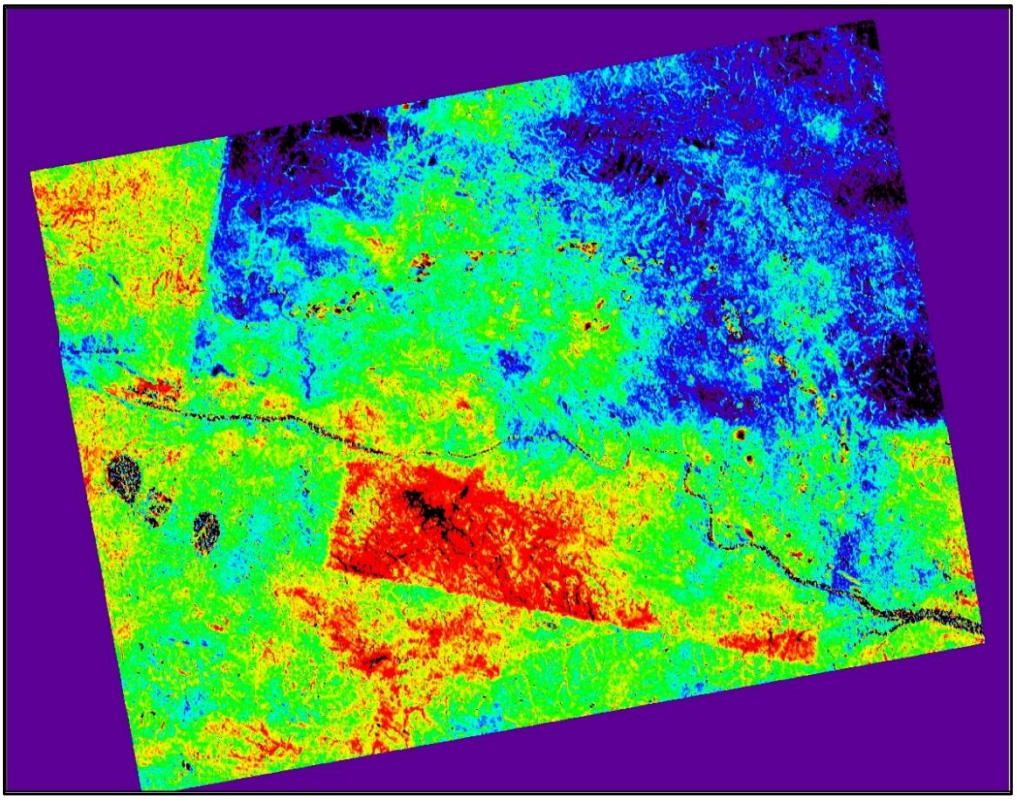

Figure C-2: Filtered image pair (10118-11460)

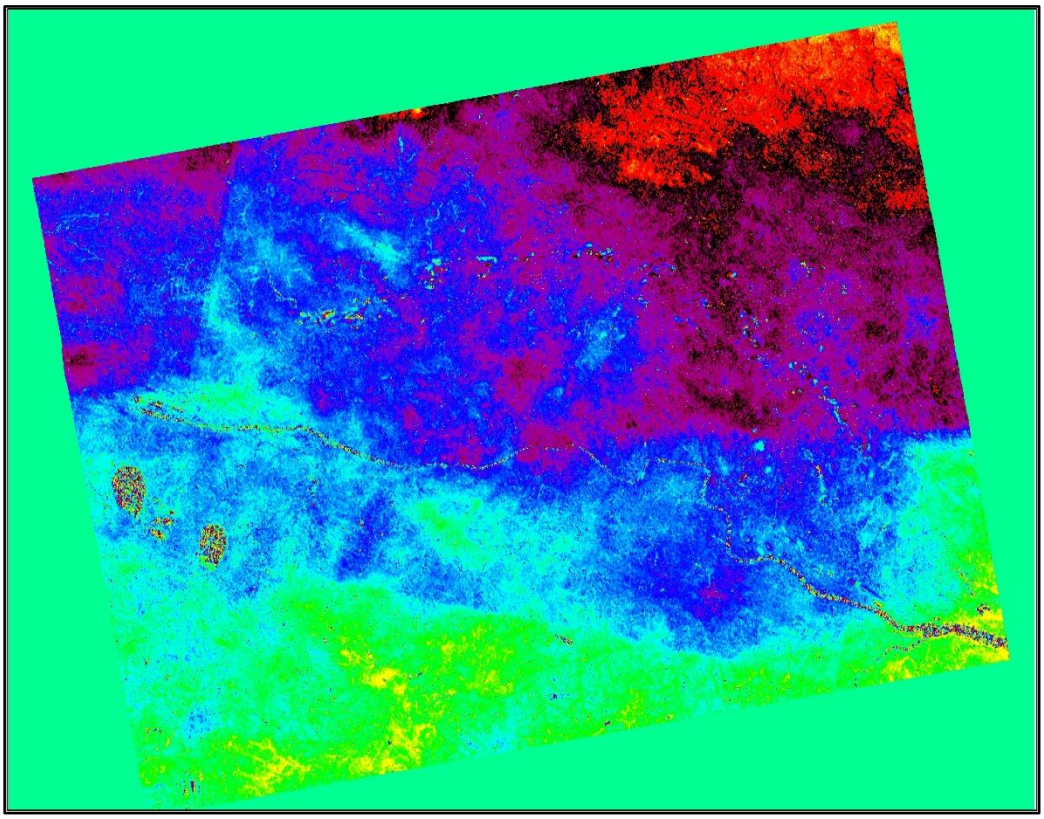

Figure C-3: Filtered image pair (10789-21525)

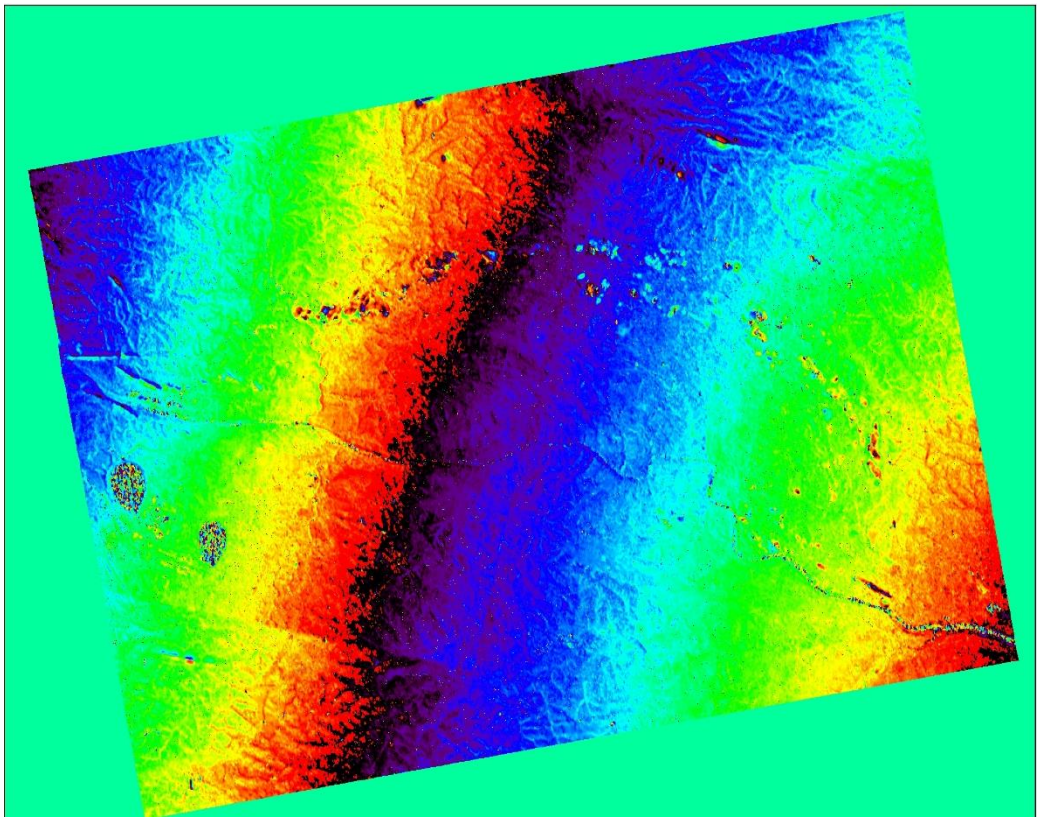

Figure C-4: Filtered image pair (20854-21525)

APPENDIX-D

UNWRAPPED IMAGES

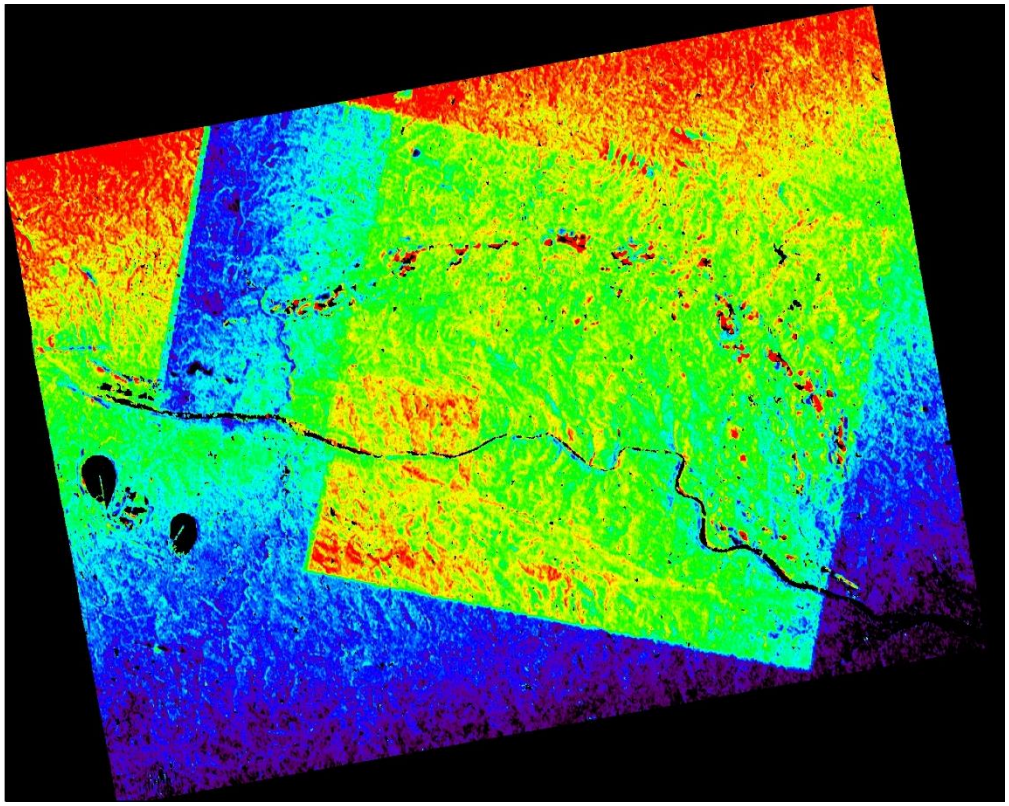

Figure D-1: Unwrapped image (10118-10789)

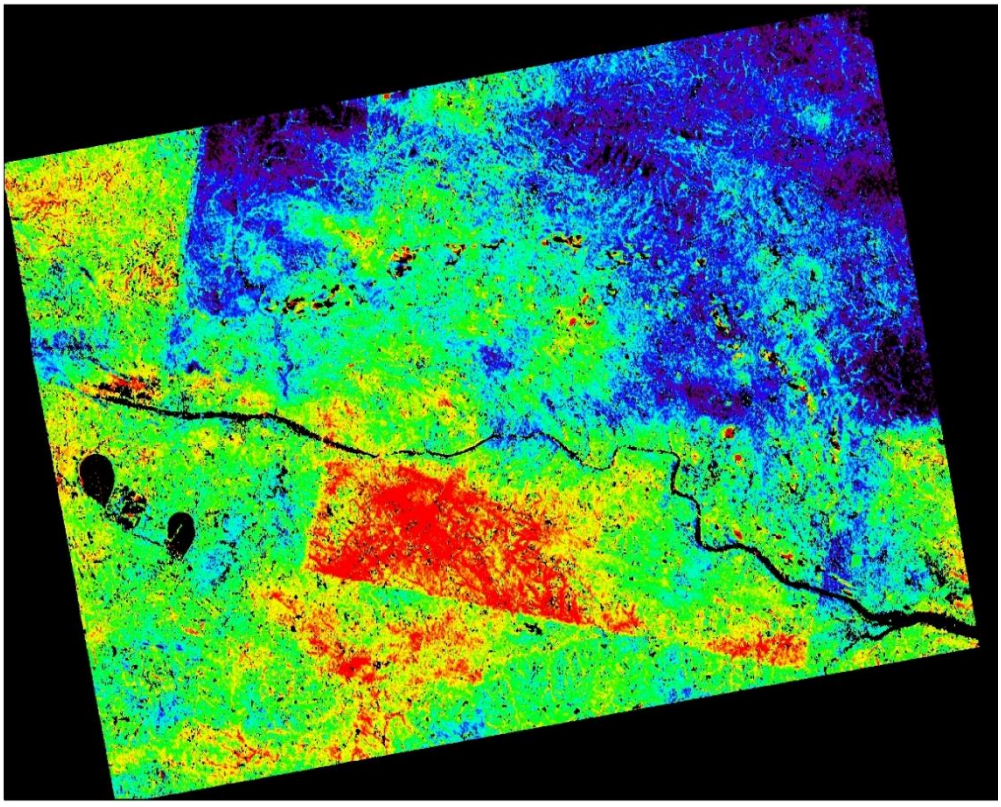

Figure D-2: Unwrapped image (10118-11460)

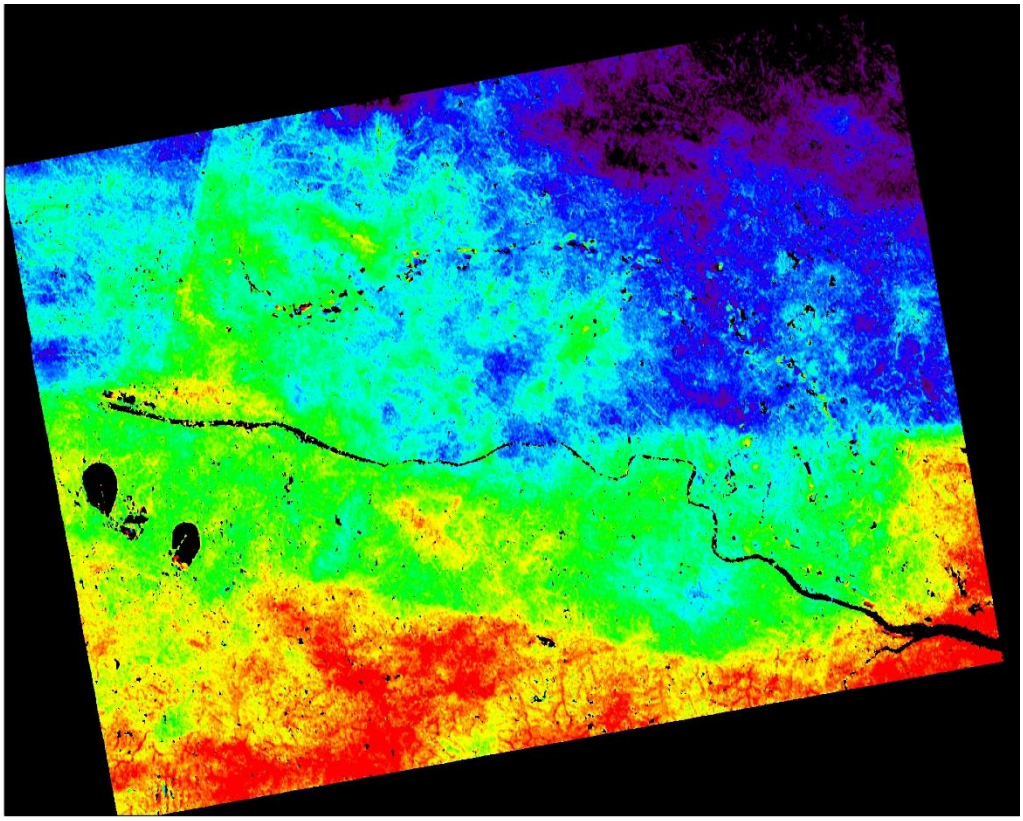

Figure D-3: Unwrapped image (10789-11460)

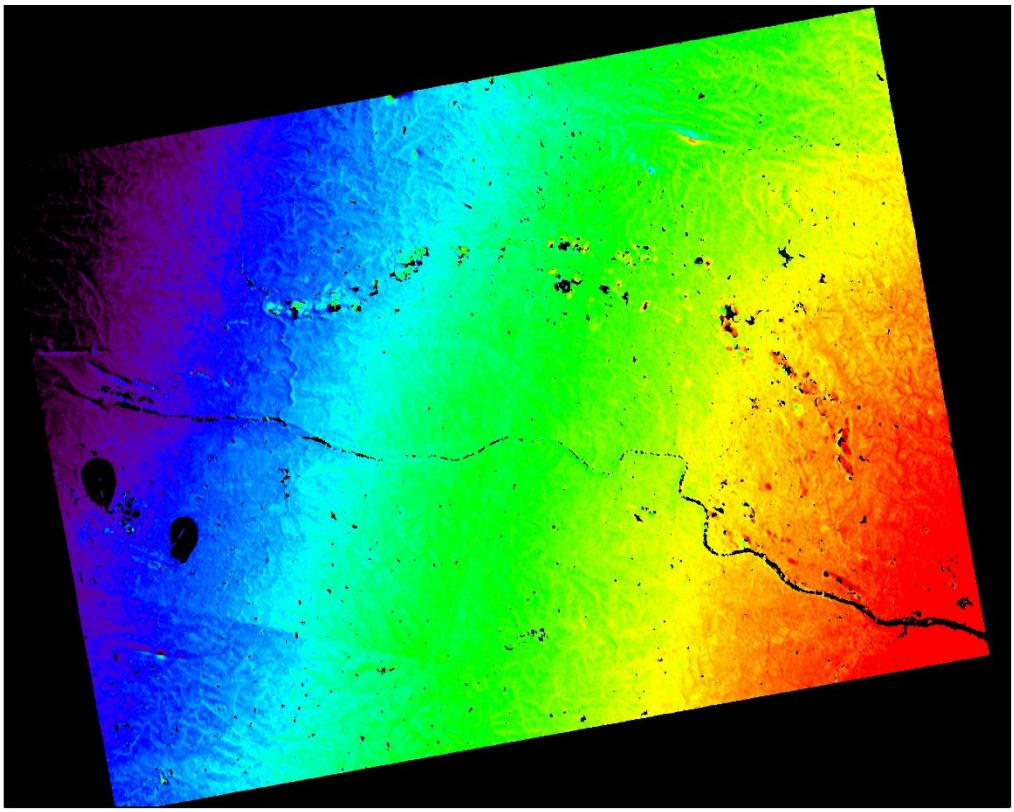

Figure D-4: Unwrapped image (20854-21525)

APPENDIX-E

Subsidence fringe statistics

Table E-1: Subsidence fringe statistics

InSAR Pair (Acquisition Period)	Temporal Baseline (Days)	Fringe ID	Unwrapped Phase Statistics		Phase Difference		LOS Path Difference		Subsidence (in cm)		Area (in Km²)
			Fringe (min to max)	Background (min to max)	Max.	Average	Max.	Average	Max.	Average	
10118-10789 (Dec 07-Feb 08)	46	F1	-2.44 ± 0.65 (-4.27 to -0.58)	-3.48 ± 0.31 (-4.15 to -3.1)	2.52	1.04	4.73	1.95	4.967	2.0475	0.28
		F2(a)	-2.15 ± 0.82 (-3.37 to 0.33)	-3.15 ± 0.19 (-3.39 to -2.89)	3.22	1	6.05	1.87	6.353	1.9635	0.19
		F3	-1.79 ± 1.02 (-3.12 to 0.57)	-3.32 ± 0.16 (-3.61 to -3.08)	3.65	1.53	6.85	2.87	7.193	3.0135	0.12
		F4(a)	-2.17 ± 0.61 (-3.34 to 0.04)	-3.13 ± 0.20 (-3.58 to -2.95)	2.99	0.96	5.61	1.8	5.891	1.89	0.86
		F5(a)	-2.13 ± 0.74 (-3.16 to 0.45)	-3.0 ± 0.19 (-3.27 to -2.8)	3.25	0.87	6.1	1.63	6.405	1.7115	0.21
10118-11460 (Dec 07-Mar 08)	92	F4(b)	2.38 ± 0.62 (0.89 to 5.6)	1.77 ± 0.3 (1.32 to 2.39)	3.21	0.61	6.03	1.14	6.332	1.197	0.29
		F5(b)	1.83 ± 0.79 (0.75 to 4.63)	0.91 ± 0.13 (0.71 to 1.12)	3.51	0.92	6.59	1.72	6.92	1.806	0.18
		F6	2.87 ± 0.66 (1.81 to 4.21)	2.04 ± 0.2 (1.73 to 2.46)	1.75	0.83	3.2	1.55	3.36	1.6275	0.13
		F7	2.38 ± 0.9 (1.32 to 4.41)	1.4 ± 0.3 (0.83 to 1.76)	2.65	0.98	4.9	1.84	5.145	1.932	0.04
		F8	2.87 ± 0.76 (1.68 to 5.07)	1.75 ± 0.22 (1.35 to 2.17)	2.9	1.12	2.1	2.1	2.205	2.205	0.24
		F9	2.77 ± 0.85 (1.56 to 4.9)	1.75 ± 0.3 (1.02 to 2.03)	2.87	1.02	5.39	1.91	5.66	2.0055	0.16

InSAR Pair (Acquisition Period)	Temporal Baseline (Days)	Fringe ID	Unwrapped Phase Statistics		Phase Difference		LOS Path Difference		Subsidence (in cm)		Area (in Km²)
			Fringe (min to max)	Background (min to max)	Max.	Average	Max	Average	Max.	Average	
10789-11460 (Feb 08-Mar 08)	46	F10(a)	0.21 ± 1.4 (-3.7 to 2.57)	-0.81 ± 0.63 (-2.61 to -0.26)	2.83	1.02	5.31	1.91	5.576	2.0055	0.15
20854-21525 (Dec 09-Feb 10)	46	F2(b)	-2.84 ± 1.73 (-6.01 to -0.07)	-3.2 ± 0.66 (-4.22 to -2.06)	1.99	0.36	3.73	0.67	3.917	0.7035	0.03
		F10(b)	-1.67 ± 0.64 (-2.8 to 0.19)	-2.76 ± 0.21 (-3.25 to -2.49)	2.68	1.09	5.03	2.04	5.282	2.142	0.22

APPENDIX-F

GROUND TRUTHS OBSERVED DURING FIELD VISIT

Figure (a), (b), (c) and (d) shows coal fire affected areas. The areas encircled in red colour are the cracks from where the smock comes out.